Mapping of surface radiogenic heat production from in situ gamma spectrometry and chemical data of exhumed mantle peridotites at the St. Peter and St. Paul archipelago (equatorial Atlantic)

Thomas Ferreira da Costa Campos, José Humberto Araujo, Susanna Eleonora Sichel, Valéria Fonseca da Silva Pastura, Kenji Freire Motoki, Leonardo Mairink Barão, Marcia Maia, Estefan Monteiro da Fonseca, Julio Navoni, Thais Vargas, et al.

▶ **To cite this version:**

Thomas Ferreira da Costa Campos, José Humberto Araujo, Susanna Eleonora Sichel, Valéria Fonseca da Silva Pastura, Kenji Freire Motoki, et al.. Mapping of surface radiogenic heat production from in situ gamma spectrometry and chemical data of exhumed mantle peridotites at the St. Peter and St. Paul archipelago (equatorial Atlantic). Applied Radiation and Isotopes, 2023, 192, pp.110608. 10.1016/j.apradiso.2022.110608 . hal-04241495

HAL Id: hal-04241495
https://hal.science/hal-04241495v1

Submitted on 17 Oct 2023

HAL is a multi-disciplinary open access archive for the deposit and dissemination of scientific research documents, whether they are published or not. The documents may come from teaching and research institutions in France or abroad, or from public or private research centers.

L'archive ouverte pluridisciplinaire **HAL**, est destinée au dépôt et à la diffusion de documents scientifiques de niveau recherche, publiés ou non, émanant des établissements d'enseignement et de recherche français ou étrangers, des laboratoires publics ou privés.

Journal Pre-proof

Mapping of Surface Radiogenic Heat Production from in situ Gamma Spectrometry and Chemical Data of Exhumed Mantle Peridotites at the St. Peter and St. Paul Archipelago (Equatorial Atlantic)

Thomas F. da C. Campos[a]*, José H. Araujo[b], Susanna E. Sichel[c], Valéria F. S. Pastura[d]; Kenji F. Motoki[c], Leonardo M. Barão[e], Marcia Maia[f], Estefan M. Fonseca[c], Julio Navoni[a], Thais Vargas[g], Peter Szatmari[h] and Daniele Brunelli[i]

[a]Department of Geology of Federal University of Rio Grande do Norte, 59078-970 Natal, Rio Grande do Norte, Brazil

[b]Department of Geophysics, Federal Fluminense University, Niteroi, 24210-240 Rio de Janeiro, Brazil

[c]Department of Physics of Federal University of Rio Grande do Norte, 59078-970 Natal, Rio Grande do Norte, Brazil

[d]Nuclear Engineering Institute, Rio de Janeiro, 21941-614 Rio de Janeiro, Brazil

[e]Department of Geology of Parana Federal University, Curitiba, 80060-240 Parana, Brazil

[f]European Institute of the Sea - Oceanic Domain of University of Western Brittany, Plouzané/Brest, 29280, France

[g]Department of Mineralogy and Igneous Petrology of Estate University of Rio de Janeiro, 20550-900 Rio de Janeiro Brazil

[h]Leopoldo Américo Miguêz de Mello Research and Development Center (CENPES/PETROBRAS), Rio de Janeiro, 21941-915 Rio de Janeiro Brazil

[i]Department of Chemistry and Geology of University of Modena and Reggio Emilia, 41125 Italy

*e-mail: thomas.campos@ufrn.br

Journal Pre-proof

Journal Pre-proof

ABSTRACT

This work presents the first mapping of the radiogenic heat production (RHP) and the respective radiogenic heat flow (RHF) of the Saint Peter and Saint Paul Archipelago (SPSPA) located at 1°N in the Equatorial Atlantic Ocean. Using radiogenic heat producing elements (RPE) we inferred a radiogenic heat production ranging 0.08-0.68 $\mu W/m^3$ (Median: 0.21 $\mu W/m^3$ and Geometric mean: 0.25 $\mu W/m^3$) by whole-rock chemical analysis and between 0.08 and 0.48 $\mu W/m^3$ (Median: 0.19 $\mu W/m^3$; Geometric mean: 0.19 $\mu W/m^3$) by in situ Gamma radiation spectrometry. The mean of radiogenic heat production of mylonite rocks from SPSPA (0.22 $\mu W/m^3$) is significantly higher than predicted values for ultramafic rocks as those largely outcropping in the SPSPA. This is probably due to the pervasive alteration of these rocks and the incorporation of little magma fractions during mylonitization. By converse, the average surface radiogenic heat flow (49.7 $\mu W/m^2$) is lower than that predicted for the oceanic lithosphere, suggesting that the upper mantle contribution to the heat flow is also low in the SPSPA region. Based on the acquired data and the peculiar tectonics of the SPSPA we propose that the lithospheric mantle around the SPSPA area is colder than that surrounding the Equatorial Atlantic region.

Keywords: Radiogenic Heat Production; Radiogenic Heat Flow; Abyssal peridotite; St. Peter and St. Paul Archipelago; Equatorial Atlantic

Journal Pre-proof

Journal Pre-proof

1. INTRODUCTION

The heat transfer from the Earth's interior to the surface is supplied variously by the primordial heat accumulated during early planetary accretion, subsequent segregation and crystallization of the Earth's mantle-core and by the radioactive decay of heat-producing elements (HPE) within the Earth [1]. Among the HPEs, only the primordial radionuclides having disintegration half-lives similar to the Earth's age are still contributing to the global heat flux from the Earth's interior. About 98% of the current heat production is associated with the radioactive decays series of U-238 (half-life ≈ 4.5 Ga) and Th-232 (half-life ≈14 Ga) and the decay of K-40 (half-life ≈1.3 Ga). Another uranium isotope that also contributes to the heat production is U-235, but due to its shorter half-life (≈ 0.7 Ga), its residual mass is estimated now reduced to 0.7% of the total Earth's uranium. A part for potassium and the uranium-thorium decay series the other long half-life radioactive isotopes have a negligible contribution to the global Earth heat because of their very slow decay rates (e.g.: Rb-87: ≈ 49 Ga and Sm-147: ≈ 106 Ga). At the beginning of Earth's formation, some other radioactive isotopes with short half-lives made a significant thermal contribution, but their mass is currently undetectable [2].

Part of the Earth's heat is dissipated from the mid Ocean Ridges during the creation of the oceanic lithosphere and plays a significant role in the global oceanic heat flow. The ridge crest heat loss can be on the order of 45% of the total Earth's heat flow, while heat loss through the continents is estimated ranging 30 - 40% [3, 4, 5, 6, 7, 8].

The occurrence of ultramafic rocks in the oceanic environment is reported from different tectonic settings both axial ridges [9, 10] and transforms [11, 12, 13, 14, 15]. Texturally ultramafic rocks record extremely variable degrees of deformation from lithospheric mantle diffuse deformation [16] to focused mylonitization as well expressed in the rocks from the SPSPA. All oceanic ultramafics usually go through a pervasive serpentinization and halmyrolisis due to shallow interaction with the hydrothermal fluids [17, 18, 19, 20, 21]. The portion of upper mantle incorporated into the lithosphere is about 100 km thick [22, 23, 24] while in the oceans ranges from 30 km below the ridges to continental thicknesses in the old crustal regions [24].

The St. Peter and St. Paul Archipelago, in the Equatorial Atlantic, is situated at 0°55'N, 29°20'43"W and pertains to Brazil. It consists of a small group of islets (5) and rocks (5) standing above an active transform fault (Figure 1), whose migrating tectonics has generated the uplift of a transverse sigmodal ridge, named Atobá Ridge, surfacing in the SPSPA rocks [25].

The first report on the peculiarity of this archipelago is due to C. Darwin during the voyage of the H.M.S. Beagle (1831-36) [26, 27]. He recognized the non-volcanic nature of the SPSPA, in that differing from all other mid-oceanic islands: "…Is not this the first Island in the Atlantic which has been shown not to be of volcanic origin?" (Darwin, notes on-board the Beagle, February 16th, 1832). The lithological composition of the islands has been later described as peridotite mylonite and serpentinized peridotite mylonite [28, 29, 30, 31].

The Atobá Ridge [25] is formed by two different geological domains designated as North and South Ridges separated by the northern transform fault of the St. Paul transform system [25, 31]. This E-W trending fault, presents a step-over in the middle of the Atobá ridge, whose eastward migration is responsible for the onset of the transpressive tectonics that uplifted the Atobá ridge. In this tectonic system, two different slices of lithosphere were emplaced pertaining to different tectonic plates (Nubia and South America) and generating a regional swollen positive flower structure [25]. By looking at the 3500 m depth contour line, the whole structure appears as an elongated sigmoid about 90 km long and

20 km wide [30]. The North Ridge is formed by highly mylonitized and serpentinized peridotite with abundant block faulting while the South Ridge is relatively less deformed [30, 31]. The rock assemblage of the SPSPA is unusual relative to common oceanic ultramafic rocks because of the association of highly mylonitized ultramafic mantle rocks, predominantly abyssal spinel peridotite with kaersutite-rich rocks (Figure 2), that show high concentrations of the Light Rare Earth Elements, K_2O and TiO_2 [32, 33, 34, 35, 36, 37, 38].

The origin of the SPSPA is interpreted as deriving by the combined effect of cataclastic diapirism and differential strike-slip and pull-apart faulting along the St. Paul Transform Zone, which sequentially unroofed mantle exposed by footwall uplift [25, 30]. This hypothesis was confirmed by [39] based on the C-14 age measurements on the Holocene waterline and subtidal deposit from SPSPA which indicated near-steady uplift during the last 6,600 years at an average rate of ≈ 1.5 mm/yr. Tele-seismic evidences also suggest that the uplift acted intermittently. Recently, the alkali-rich peridotite cropping out on the Atobá Ridge has been suggested to derive by a process of refertilization of residual mantle peridotite by ion-exchange reactions between alkaline magma and mantle rocks under asthenospheric to lithospheric conditions [36, 37, 38].

The present paper reports the surface radiogenic heat production (RHP) based on whole-rock chemical analyses and in situ gamma radiation spectrometry (*is*GRS) from the St. Peter and St. Paul Archipelago, Equatorial Atlantic, Brazil.

2. GEOLOGICAL BACKGROUND

The SPSPA lays about 100 km north to the equator line in the Atlantic Ocean (Figure 1) and is the summit of the Atobá Ridge, a 3,700 m prominent ridge exhumation of the oceanic lithospheric mantle by a transpressive tectonics [25, 40]. The SPSPA is composed of 5 islets (Belmonte, Northwest, Northeast, Southeast and South) and 5 rocks (Beagle, Pilar, Cambridge, Coutinho and Cabral), following the names given by [41] and the nautical map of SPSPA publishing by Brazilian Navy), with a total emerged area of ≈ 17,000 m2.

The NW portion of Belmonte islet is dominated by homogeneous aphanitic mylonite, light grey to grey-greenish in color. In contrast, the SW part of Belmonte and other islets are essentially composed of heterogeneous aphanitic rock, showing a range of color between greenish dun and light tan. The homogeneous aphanitic rock is a mylonitized peridotite (Figure 2 and 3a) while the heterogeneous aphanitic domains result from variable degrees of serpentinization of the peridotite mylonite. The serpentinization process developed preferentially along the joints, leading in many places to the total replacement of the pre-existing mylonite rock [31] (Figure 2). Kaersutite-rich mylonite dikes with white carbonate veins outcrop in the east side of Southeast islet (Figure 2 and 3a). This mylonite contains kaersutite (> 90%), Fe-Ti oxides, scapolite, allanite, white carbonate, sulphides and zeolites. In the Southeast, Northeast and more rarely in South islets outcrops are mainly represented by a layered mylonite with millimeter to decimeter interlayered kaersutitic and peridotitic layers (Figure 2 and 3b, c, d). Thick peridotitic layers are petrographically identical to the mylonitic peridotites outcropping in the other islets. The kaersutite mylonite show millimeter-thick veins of carbonate (Figure 3c, d). This layered kaersutite-peridotite mylonite (Figure 3b) possibly corresponds to segregations during dynamic recrystallization after the alkaline metasomatism of mantle rocks adjacent to melt conduits and crystalized fluid in dike conduits [32, 33, 34, 35, 36, 37].

Figure 1: Location of St. Peter and St. Paul Archipelago, Equatorial Atlantic, Brazil. Figure made with GeoMapApp (www.geomapapp.org) [42].

Figure 2: Geologic map of St. Peter and St. Paul Archipelago, Equatorial Atlantic, Brazil. Color for Geologic Maps according to the U.S. Geological Survey (https://mrdata.usgs.gov/catalog/lithclass-color.php). Based from [31, 39].

Figure 3: Hand samples from St. Peter and St. Paul archipelago (Equatorial Atlantic, Brazil): A) Peridotite mylonite; B) Kaersutite mylonite with white carbonate veins; C) Serpentinized peridotite mylonite: C1- Superficial crust sample without serpentine due to the sea-water erosion; C2- Inner surface of C1, D) Layered Kaersutite-Peridotite mylonite: D1- Superficial crust sample, D2- Inner surface of D1.

3. MATERIALS AND METHODS

We collected 106 samples from the largest islets and rocks, representative of all mantle-derived lithologies present in the archipelago (Figure 4a) and these rocks are a mixture of peridotite, serpentinite and kaesurtite, derived from the different geological processes that gave rise to the SPSPA, therefore geochemistry is possible to make a statistic correlation and kriging interpolation technique between their chemical compositions and in situ gamma radiation spectrometry (isGRS) [31, 35, 36, 37, 38]. The rocks were sampled in a random distribution, 10 to 20 cm below the surface, to reduce the effects of halmyrolise, meteoric alteration and guano decomposition. The *is*GRS was measured on 300 points upon the rocks, with a sampling time of 360 seconds following the recommended methodologies of the International Atomic Energy Agency (IAEA) for low radioactivity outcrops, using a gamma spectrometer model RS-230 (BGO crystal) from Radiation Solution (Figure 4b). Bulk rock chemical analyses were done at ALS-CHEMEX Laboratory (Vancouver, Canada) and trace element concentrations by ICP-AES (Varian/Vista) and ICP-MS (Perkin-Elmer/ELAN-800). The bulk rock specific densities were measured by QUANTACHROME ULTRAPYC 1200e with 10 cm^3 cell (Accuracy: < ± 0.03% g/cm^3; Repeatability < ± 0.015% g/cm^3).

SPSPA are small (≈ 17,000 m^2), whose islands are close together and gamma radiation background was measured over a wooden fishing boat, c. 8 km away from the archipelago in the Atlantic Ocean (30°1'W 0°35'N). The 30 nGy/h of background was subtracted from all gamma radiation measurements.

Table 1 show heat-production element (HPE) by whole-rock chemical analysis and Table 2 show HPE by *is*GRS of mylonite rocks from SPPA.

Figure 4: Sampling: A) Rock sample location (n: 106); B) Radiometric measurement location (n: 300).

4. RESULTS AND DISCUSSION

4.1. Comparison among whole-rock chemistry and in situ gamma radiation spectrometry

The comparison of *is*GRS and ICP-MS results are shown in Table 3 and plotted in Figure 5. U and Th measured with *is*GRS while showing a linear and strong correlation with ICP-MS-derived concentrations

present a significant to higher values (Figure 5), K does not show a significant correlation due to its extremely low concentration in ultramafic rocks.

Table 3: Linear regression coefficients of ICP-MS versus *is*GRS values of U and Th given in Table 1.

Figure 5: Comparison among ICP-MS and *is*GRS of U and Th values of peridotite and kaersutite mylonites rocks from SPSPA, Equatorial Atlantic, Brazil.

4.2. Mapping Surface Heat-producing Elements by Chemical Analyse

We made a raster surface color map by interpolating the contents at the sampling points of the heat-producing elements (HPE) using the Kriging technique. Figure 6 shows the kriging surface color maps of surface HPE concentrations by whole-rock chemical analyses (U and Th in ppm, K in %).

Figure 6: Kriging surface color map of surface HPE by whole-rock chemical of peridotite and kaersutite mylonite rocks from SPSPA: A) Uranium (ppm); B) Thorium (ppm); C) Potassium (%). White line: geological contact.

4.3. Surface Heating-producing Elements by In situ Gamma Radiation Spectrometry

The Figures 7 show a Kriging surface color map of surface HPE concentrations disintegration (Bq/sec) from in *is*GRS (U and Th in Activity Equivalent ppm, K in Activity Equivalent %)

Figure 7: Kriging surface color map of surface HPE by *is*GRS of peridotite mylonites rocks from St. Peter and St. Paul archipelago (Equatorial Atlantic, Brazil): A) Disintegration (Bq/sec); B) Uranium (Activity Equivalent ppm); C) Thorium (Activity Equivalent ppm); D) Potassium (Activity Equivalent %). White line: geological contact.

4.4. Surface Radiogenic Heat Production

The surface radiogenic heat production (SRHP: A_0) of a given rock sample was estimated using the empirical equation (1) [43, 44, 45, 46]:

$$A_0 = 10^{-5}\,\rho\,(9.51C_U + 2.56C_{Th} + 3.50C_K \qquad (1)$$

Where: A_0 is SRHP of the rock ($\mu W/m^3$), ρ is rock density (kg/m^3) and C_U and C_{Th} in AE-ppm and C_K in AE-% and are the heat-producing element contents.

Journal Pre-proof

We calculate the SRHP (A_0) for both HPE obtained by whole-rock chemical analysis, as well as *is*GRS. The average A_0 results are summarized in Table 4 and illustrated as a kriging surface color map of the radiogenic heat production in Figure 8.

Table 4: Statistical synthesis of SRHP (A_0: μWm^3) results from mylonite rocks of SPSPA. Max: Maximum; Min: Minimum; GM: Geometric mean; Med: Median; SD: Standard Deviation.

Figure 8: Kriging surface color map of SRHP (A_0) of mylonite rocks from SPSPA obtained by whole-rock chemical analysis (A) and by in situ gamma radiation spectrometry (B). White line: geological contact.

The A_0 rates for such units are similar, despite the discrepancy in some samples, where we have lower levels of chemical analysis than the equivalent activity in situ gamma spectrometry levels (Figs 5, 6, 7 and 8). It is plausible that inhomogeneous distribution was caused by overlapped complex differentiation processes (e.g.: different halmirolyse, serpentinization and carbonatation degrees and the secular radioactive disequilibrium due to alteration process). It should be noted that the peridotite mylonite with the highest degree of serpentinization and carbonatation were those with the highest contents of uranium.

The serpentinization and carbonatation process are generated by the pervasive hydration of mantle rocks due to hydrothermal circulation during the formation of the oceanic crust and mantle exhumation [47, 48, 49, 50, 51, 52, 53, 54], serpentine minerals replace olivine and pyroxenes of the original rock while carbonates accumulate in late, lower temperature veins [31, 55]. In general, the serpentinized mantle rock, despite their low trace element concentration, are often enriched in some incompatible and fluid-mobile elements (FME), these elements are carried by hydrothermal fluids originated from seawater and modified during the circulation in the oceanic crust [55, 56, 57, 58].

The mylonite mantle rocks from SPSPA are known to be enriched in incompatible elements by alkaline metasomatism, namely light-REE, which suggests the metasomatism by hydrothermal fluids and/or melt percolation [31, 32, 34, 35, 36, 37, 38].

Extended trace element patterns normalized to the primitive mantle (PM) of mantle rocks from SPSPA show that serpentinized and halmyrolised peridotite mylonite is characterized by U, Pb and Sr enrichment (Table 5; Figure 9a) with no significant enrichment in Th. This is consistent with the U soluble nature in fluids [59].

The average FME abundances in serpentinized peridotite mylonite are normalized to the Primitive Mantle and show in Figure 9b (Table 5), which indicates a significant enrichment in U and Pb but also in Ca, Sr, Sb and As. This fact can be explained by the occurrence of carbonate in the whole rock budget and carbonates are known to host U (0.142– 0.655 ppm) [60]; 2–4 ppm; [61] and Pb (0.139–3.05 ppm) [62]; ≈9 ppm [63]. As and Sb are known to be mobile in aqueous fluids for temperature ranging between room temperature and 500° C, as observed with the high concentrations of As in surface, ground and seawaters [63, 64], consequently during serpentinization process these are released from the hydrothermal seawater derived fluid and are then incorporated in the serpentine layer.

Journal Pre-proof

4.5. Surface Radiogenic Heat Flow

It is accepted that the surface radiogenic heat flow (SRHF: q_s) of an area has a linear correlation with SRHP (A_0) [65, 66, 67, 68] as expressed by equation (2):

$$q_s = q_r + A_0 D \quad (2)$$

Where q_r is the reduced heat flow, A_0 is the SRHP based on the HPE data in $\mu W/m^3$ and D is the thickness of the upper crust HG layer. The reduced heat flow (q_r) represent the heat flux from the mantle or Moho and the product AD is the radiogenic HF in the upper crust. Therefore, the q_s - A_0 relationship corresponds to a partition of the total surface heat flow among the basal heat flow (q_r), that is, the average heat flow at depth D of the crust (upper mantle or Moho) plus the of additional radiogenic heat flow produced at the top of crust with thickness D. Therefore, basal heat flow (q_r) represents an increasing fraction of surface heat flow.

Table 5: Average trace and major elements of rocks from SPSPA. *: below limit detection; LOI: Lost on ignition

Figure 9: Primitive Mantle normalized spider-diagram [69] for A) Peridotite mylonite rocks from SPSPA; B) Normalized concentrations of fluid-mobile and fluid-immobile elements in peridotite mylonite from SPSPA. Fluid-mobile elements refer to those with high solubilities in aqueous fluids, to clarify the diagram Fluid-immobile elements are listed in order of compatibility with mantle minerals during partial melting.

To understand the origin of the surface heat source in the area of SPSPA, we consider the Sclater-Francheteau model for the oceanic lithosphere and the reduced heat flows (q_r) of the lithosphere layers (Figure 10) defined by the authors [23]. This model provides for a 120 km thick lithosphere plate, constituted as follows: 5 km of a basalt layer with RHP of 0.5 $\mu W/m^3$ + 15 km of peridotite layer with a RHP of 0.01 $\mu W/m^3$ (D layer) and a 100 km of "Pyrolito I" layer (a mixture of one part basalt with three parts ultramafic peridotite [70]) with a RHP of 0.13 $\mu W/m^3$.

The RHP of this model generates a RHF on the surface of 4.6x10-5 $\mu W/m^2s$, thus distributed about 1.7 $\mu W/m^2s$ comes from the lithosphere and 2.9 $\mu W/cm^2s$ from the Mantle (Pyrolite I), whose average RHP is 0.04 $\mu W/m^3$, with a RHF of 16.7 $\mu W/m^2s$, at a depth of 400 km (Pyrolite II; [70]). However, as there is no general model of radioactive heat generation for the lithosphere because it is impossible to characterize all the geographic regions of the continents and ocean [71, 72, 73, 74, 75].

For the q_s calculations (Equation 2) we assumed that the contents of the HPE are normally distributed, the reduced heat flow (q_r) from the lithospheric layer is 4.6 x 10-5 μWm^2s and for the D we consider the thickness of 15 km, because the Atobá ridge is a made by a thick mantle uplift and do not show a basaltic layer as normally present in the oceanic crust [25], consequently the thickness of D layer is much smaller than the scale of horizontal fluctuation in radioactivity, the effect of lateral heat

production variation on q is negligible, because there are no lateral contribution from the heat production by other rocks (Table 6 and Fig. 1).

Table 6: Statistical synthesis of RHF (q_s: $\mu W/m^2s$) results from mylonite rocks of SPSPA. Max: maximum; Min: Minimum; GM: Geometric mean; MED: Median; SD: Standard Deviation. *is*GRS: in situ gamma ray spectrometry.

Figure 10: Oceanic lithosphere and continental shield model, assuming a constant flux at 200 km depth. The heat flow at different levels is indicated by black thick arrows. Based on [23]

The radioactive heat production (RHP) in a given area is controlled by the heat production element (HPE) distribution. The uranium, thorium and potassium equivalent levels in the SPSPA mylonites were measured by both chemical analysis and in situ gamma radiation spectrometry (Tables 1 and 2, Figures 5 and 6). Given the location of the studied samples, they are representative of the superficial or apparent values. However, the surface HPE and surface RHP (A_0) calculated by the two methods within the same geological unit are proportionally similar, despite the discrepancy in some samples, where we have lower levels of HPE by chemical analysis than the equivalent activity *is*GRS levels. The area possesses a range of surface RHP varying from 0.08 to 0.68 μWm^3 by whole-rock chemical analysis and from 0.08 to 0.48 μWm^3 by *is*GRS (Table 4, Figure 7 and 8).

The higher level A_0 is supported by field observations, indicative of the increase of uranium and potassium levels during serpentinized (high U), halmyrolised (high U and K) and metasomatism (kaersutite enrichment: high K). These observations present an association to faults and lineaments (Figure 2 and 11).

The radioactive heat production may exhibit some irregularity due to the dissimilarity in the geochemical behaviour of U, Th and K during geological processes which determine the HPE distribution. It is plausible that the inhomogeneous distribution of A_0 was caused by overlapped complex differentiation processes (e.g.: different degrees of metasomatism, serpentinization, halmirolyse alteration and the secular radioactive disequilibrium provoked by alteration).

The calculated average of the surface RHP of mylonite rocks from SPSPA (Table 1) are higher than the average surface RHP of crustal rocks and lithospheric mantle published by [76] 0.01 $\mu W/m^3$, [62] 0.02 $\mu W/m^3$, [77] 0.099 $\mu W/m^3$, [78] 0.013 $\mu W/m^3$, [79] 0.024 $\mu W/m^3$ and [80] 0.018 $\mu W/m^3$. This is because the mylonite rocks from SPSPA suffered metasomatism that affect surface exposures during exhumation and/or near-surface groundwater flow that increased HPE levels, as suggested by [77] for the Jericho xenoliths on the Slave craton.

The surface RHF (q_s) mimic the surface RHP (A_0) within mylonite rocks of SPSPA and varying from 47.3 to 56.4 $\mu W/m^2s$ with Geometric mean of 50.4 $\mu W/m^2s$ (Median: 50.1, Standard deviation: 2.31) by whole-rock chemical analysis and from 47.4 to 53.3 $\mu W/m^2s$ with Geometric mean of 49.0 $\mu W/m^2s$ (Median: 48.2, Standard deviation: 0.82) by in situ gamma radiation spectrometry (Table 2 and 6; Figure 11)

Figure 11: Kriging surface color map of surface radiogenic heat flow (q_s: $\mu W/m^2s$) of mylonites rocks from SPSPA obtained by whole-rock chemical analysis (A) and in situ gamma radiation spectrometry (B). White line: geological contact.

Although the RHP from the mylonite rocks from SPSPA is high, the respective average radioactive heat flow is relatively low (49.7 $\mu W/m^2s$) when compared with suggested average oceanic heat flux, which ranges within 80 to 101 $\mu W/m^2s$ [1, 23, 78, 79, 80] .This is also in agreement with [81] who stated that is probably the largest source of heat in the earth's crust and other sources may be important in specific locations. Therefore, we can suggest that the most likely source of radioactive heat flow in the SPSPA area appears to be associated with only heat from the upper mantle.

Although the HPE from SPSPA is relatively higher than those predicted for ultramafic rocks, the HF from radioactive disintegration is relatively lower than those predicted for the oceanic crust. This suggests that the RHF from the upper mantle in the SPSPA area is relatively low compared to the RHF upper from upper mantle of other areas in the oceanic crust.

Several geological evidences demonstrate that the upper mantle of the SPSPA area is colder than the upper mantle outside the Equatorial Atlantic area, such as:

a) The existence of a melt fraction within mantle peridotite may indicate that the upper mantle is cold enough to freeze and trap any small amount of melt migrating through it (Figure 2 and 3) [36, 37];

b) The rarity of basaltic flows on Atobá ridge [25] upper mantle indicates that an upper mantle belt along the equatorial Atlantic is exceptionally cold [82, 83, 84, 85, 86];

c) The existence of transform faults relatively close to each other bounding ridge segments of small size among them, with the consequence of enhancing the cold-edge effect. The inferred equatorial pattern of cold-edge dense upper mantle could reflect down-welling mantle flow along the equatorial zone of the oceans (Figure 12)

Figure 12: Saint Paul transform system, Equatorial Atlantic. Thick red line: ridge axis; dashed red line: Active transform fault; black dashed line: inactive transform fault. Based [25].

5. CONCLUSION

We present the mapping of radiogenic heat production (RHP) and the respective radiogenic heat flow (RHF) of the St. Peter and St. Paul archiepelago, based on radiogenic heat-producing elements (RPE) data from whole-rock chemical analysis and in situ Gamma radiation spectrometry:

- ✓ The radiogenic heat production ranging from 0.08 to 0.68 $\mu W/m^3$ (Median: 0.21 $\mu W/m^3$ and Geometric mean: 0.25 $\mu W/m^3$) by chemical analysis and among 0.08 to 0.48 $\mu W/m^3$ (Median: 0.19 $\mu W/m^3$; Geometric mean: 0.19 $\mu W/m^3$) by in situ Gamma radiation spectrometry;
- ✓ The high values of surface HPE, surface RHP (A_0) and surface RHF (q_s) are locally associated with areas which show high serpentinization and halmyrolisis degree;

- ✓ The average radioactive heat production of mylonite rocks of 0.22 $\mu W/m^3$ is significantly high about those predicted for ultrabasic rocks, due to geological alteration process;
- ✓ The respective average surface radiogenic heat flow of 49.7 $\mu W/m^2s$ is to lower concerning those predicted for the oceanic lithosphere, which indicates that the additional heat flow from of the upper mantle is also low in the SPSPA area;
- ✓ Our data along with tectonic features suggest that lithospheric mantle around the SPSPA area is colder than the upper mantle outside the equatorial Atlantic region.

ACKNOWLEDGEMENTS

This paper was significantly improved by review from Dr. Léo Afraneo Hartmann (Federal University of Rio Grande do Sul, Geology Department, Brazil). We would like to thank Dr. Farinha Ramos (Mining and Geological Institute of Portugal), Dr. Annika Dziggel (Institute für Mineralogie und Lagerstättenlehre, Rheinisch Westfälische Technische Hochschule -Aachen, Germany) and Dr. Thomas Thyer (Institut für Mineralogie, Universität Stuttgart, Germany) for providing most of the electron probe and QEMSCAN analyses of minerals. This research was carried out in the Archipelago Programme of Interministerial Secretariat Commission for Marine Resource (SECIRM, Brazilian Government) and a grant from National Resource Committee (CNPq), Petroleum of Brazil (PETROBRAS/CENPES), Geosciences Institute of Coimbra University (Portugal), and Daniele Brunelli is supported by the Italian Programma di Rilevante Interesse Nazionale (PRIN_2017KY5ZX8).

Journal Pre-proof

423 REFERENCES

424 [1] Pollack H.N., Hurter S.J. and Johnson J.R. 1993, Heat flow from the Earth's interior: analysis of the
425 global data set. Rev. Geophys. 31:267–80

426 [2] Faure, G. 1986, Principles of Isotope Geology, 2nd edn. Wiley, New York, 589 pp.

427 [3] McKenzie, D. P. and Sclater, J. G. 1969, Heat flow in the eastern Pacific and sea floor spreading, Bull.
428 Volcanologique, 33-1, 101-1 18.

429 [4] Sleep, N. H. 1969. Sensitivity of heat flow and gravity to the mechanism of sea floor spreading, J.
430 geophys. Res., 74, 542-549.

431 [5] Pollack, H.N. and Chapman, D.S. 1977, On the regional variation of heat flow, geotherms, and
432 lithospheric thickness. Tectonophysics 38:279–96.

433 [6] Vitorello, I., Pollack, H.N. 1980, On the variation of continental heat flow with age and the thermal
434 evolution of the continents. J. Geophys. Res. 85, 983–995.

435 [7] Artemieva I.M., Mooney WD. 2001, Thermal thickness and evolution of Precambrian lithosphere: a
436 global study. J. Geophys. Res. 106:16387–414. DOI: 10.1029/2000JB900439

437 [8] Goesa, S., Hasterok, D., Schuttc, L., Klöcking, M. 2020, Continental lithospheric temperatures: A
438 review. Physics of the Earth and Planetary Interiors 306, 106-509 https://doi.org/10.1016/j.pepi.2020.

439 [9] Dick, H.J.B., 1989. Abyssal peridotites, very slow spreading ridges and ocean ridge magmatism. Geol.
440 Soc. London, Spec. Publ. 42, 71–105.

441 [10] Michael, P.J., Bonatti, E., 1985. Peridotite composition from the North Atlantic: regional and
442 tectonic variations and implications for partial melting. Earth Planet. Sci. Lett. 73, 91–104.
443 https://doi.org/10.1016/0012-821X(85)90037-8

444 [11] Wiseman, J.D.H. 1966, St Paul Rocks and the Problem of the Upper Mantle. Geophys. Journal of
445 Royal. Astronomy Society, 11, 519-525. doi.org/10.1111/j.136

446 [12] Melson, W.G. and Jarosewich, E. 1967, St. Peter and St. Paul Rocks: A High-Temperature, Mantle-
447 Derived Intrusion. Sciences 155, 1532–1535. doi.org/10.1126/science.155.3769.1532

448 [13] Bodinier, J.L.; Godard, M. 2013, Orogenic, Ophiolitic, and Abyssal Peridotites, 3rd ed, Treatise on
449 Geochemistry: Second Edition. Elsevier Ltd. doi.org/10.1016/B978-0-08-095975-7.00204-7

450 [14] Brunelli, D., Seyler, M., Cipriani, A., Ottolini, L., Bonatti, E., 2006. Discontinuous Melt Extraction and
451 Weak Refertilization of Mantle Peridotites at the Vema Lithospheric Section (Mid-Atlantic Ridge). J.
452 Petrol. 47, 745–771. https://doi.org/10.1093/petrology/egi092

453 [15] Bonatti, E., Brunelli, D., Fabretti, P., Ligi, M., Portaro, R.A., Seyler, M., 2001. Steady-state creation of
454 crust-free lithosphere at cold spots in mid-ocean ridges. Geology 29, 979–982.
455 https://doi.org/10.1130/0091-7613(2001)029<0979:SSCOCF>2.0.CO;2

456 [16] Dantas, C., Ceuleneer, G., Gregoire, M., Python, M., Freydier, R., Warren, J.M., Dick, H.J.B., 2007.
457 Pyroxenites from the Southwest Indian Ridge, 9-16 E: Cumulates from Incremental Melt Fractions
458 Produced at the Top of a Cold Melting Regime. J. Petrol. 48, 647–660.
459 https://doi.org/10.1093/petrology/egl076

[17] Lagabrielle, Y. 1998, Ultramafic-Mafic Plutonic Rock Suites Exposed Along the Mid-Atlantic Ridge Distribution and Implications for. Geophysics. Monogr. Ser. 106, 153–176. DOI: 10.1029/GM106p0153

[18] Nielson, J.E. and Noller, J.S. 1987, Mantle Metasomatism and Alkaline Magmatism. Special paper of Geological Society of America, Book 215. ISBN-10: 0813722152

[19] Snow, J. and Dick H.J.B. 1995, Pervasive magnesium loss by weathering of peridotite. Geochimica et Cosmochimica Acta, 59(20), 4219-4235. doi.org/10.1016/0016-7037(95)00239-V

[20] Alt, J.C., Shanks, W. C. 2003, Serpentinization of abyssal peridotites from the MARK area, Mid-Atlantic Ridge: Sulfur geochemistry and reaction modeling. Geochimica et Cosmochimica Acta, 67(4), 641-653, https://doi.org/10.1016/S0016-7037(02)011.42-0

[21] Mével, C., 2003. Serpentinization of abyssal peridotites at mid-ocean ridges. Comptes Rendus Geosci. 335, 825–852. https://doi.org/10.1016/j.crte.2003.08.006

[22] Bullard, E.C. 1954, The flow of heat through the floor of the Atlantic ocean. Proceeding of the Royal Society of London Series A 222: 408–422.

[23] Sclater, J.G. and Francheteau, J. 1970, The Implications of Terrestrial Heat Flow Observations on Current Tectonic and Geochemical Models of the Crust and Upper Mantle of the Earth, Geophys. J. R. Astron. Soc Volume 20/5, 509–542, doi.org/10.1111/j.1365-246X.1970.tb06089.x

[24] Sclater, J.G., Jaupart, C., Galson, D., 1980, The heat flow through the oceanic and continental crust and the heat loss of the Earth. Rev. Geophys. Space Phys. 18, 269–311.

[25] Maia, M.; Sichel, S.; Briais, A.; Brunelli, D.; Ligi, M.; Ferreira, N.; Campos, T.; Mougel, B.; Brehme, I.; Hémond, C.; Motoki, A.; Moura, D.; Scalabrin, C.; Pessanha, I.; Alves, E.; Ayres, A.; Oliveira, P. 2016, Extreme mantle uplift and exhumation along a transpressive transform fault. Nature

[26] Darwin, C. 1891, Geological observations on the volcanic islands and parts of South America visited during the voyage of H.M.S. 'Beagle', D. Appleton and Company, New York, 1891 doi.org/10.5962/bhl.title.61452

[27] Darwin, C. R. 1839, Journal of researches into the geology and natural history of the countries visited during the voyage of H.M.S. Beagle round the world, under the command of Capt. FitzRoy, R. N. Henry Colburn, London, UK.

[28] Renard, A.F. 1882, Description lithologique des récifs de St.-Paul. Extrait des Annales de la Société Belge de Microscopie. Bruxelles, Lib. Manceaux, 53 pp.

[29] Renard, A.F. 1882. On the petrology of St. Paul's Rocks. Narrative of the Challenger Report vol. 2. Great Britain Challenger Office. Printed for Her Majesty's Stationery Office, Longmans and Co. London.1882.

[30] Hékinian, R.; Juteau, T.; Gràcia, E.; Sichler, B.; Sichel, S.,; Udintsev, G.; Apprioual, R.; Ligi, M. 2000, Submersible observations of equatorial Atlantic mantle: The St. Paul Fracture Zone region. Marine Geophysical Research. 21, 529–560. doi.org/10.1023/A:1004819701870

[31] Campos, T.F.C., Sichel, S.E., Maia, M., Brunelli, D., Motoki, K., Magini, C., Barão, L.M., Vargas, T., Szatmari, P., Fonseca, E., de Melo, G., 2022. The singular St. Peter and St. Paul Archipelago, equatorial Atlantic, Brazil, Meso-Cenozoic Brazilian Offshore Magmatism. https://doi.org/10.1016/b978-0-12-823988-9.00003-4

Journal Pre-proof

[32] Roden, M.K., Hart, S.R., Frey, S.H. and Thompson, G., 1984, Sr, Nd and Pb isotopic and REE geochemistry of St Paul's Rocks: the metamorphic and metasomatic development of an alkali basalt mantle. Contr. Miner. Petrol., 85, pp. 376–390.

[33] Melson, W.G., Hart, S.R. and Thompson, G. 1972, St. Paul's Rocks, Equatorial Atlantic: Petrogenesis, Radiometric Ages, and Implications on Sea-Floor Spreading. GeologicaL Society of America, INC. Memoir, 132 132, 241–272. doi.org/10.1130/mem132-p241

[34] Frey, F.A. 1970, Rare Earth and potassium abundances in St. Paul's rocks. Earth and Planetary Sciences Letters, 7, 351–360. doi.org/10.1016/0012-821X(69)90049-1

[35] Campos, T.F.C.; Virgens Neto, J.; Amorim, V.; Hartmann, L.; Petta, R. 2003, Modificações Metassomáticas Das Rochas Milonitizadas Do Complexo Ultramáfico Do Arquipélago de São Pedro e São Paulo, Atlântico Equatorial. Geochimica Brasiliense. 17, 81–90. dx.doi.org/10.21715/gb.v17i2.201.

[36] Brunelli, D. and Seyler, M. 2010, Asthenospheric percolation of alkaline melts beneath the St. Paul region (Central Atlantic Ocean). Earth and Planetary Sciences Letters 289, 393–405. doi.org/10.1016/j.epsl.2009.11.028

[37] Brunelli, D., Paganelli, E., & Seyler, M. (2014). Percolation of enriched melts during incremental open-system melting in the spinel field: A REE approach to abyssal peridotites from the Southwest Indian Ridge. Geochimica et Cosmochimica Acta, 127, 190-203.

[38] Navon, O. and Stolper, E. 1987, Geochemical consequences of melt percolation: the upper mantle as a chromatographic column. Journal of Geology 95, 285–307. doi.org/10.1086/621620

[39] Campos T.F.C.; Bezerra, F.H.R.; Srivastava, N.K.; Vieira, M.M.; Vita-Finzi, C. 2010, Holocene tectonic uplift of the St Peter and St Paul Rocks (Equatorial Atlantic) consistent with emplacement by extrusion. Mariner Geology. 271, 177–186. doi.org/10.1016/j.margeo.2010.02.013.

[40] Barão, L.M; Trzaskos. B; Angulo, A.J; Souza, M.C. 2020, Deformation and structural evolution of mantle peridotites during exhumation on transform faults: A forced transition from ductile to brittle regime. Journal of Structural Geology 133, 22-32, doi.org/10.1016/j.jsg.2020.103981

[41] Tressler, W.L.; Bershad, S.; Berninghausen, W. 1956, Rochedos São Pedro e São Paulo (St. Peter and St. Paul Rocks). U. S. Navy Hydrographic Office Technical Report.

[42] Ryan, W. B. F.; S.M. Carbotte, J.; Coplan, S.; O'Hara, A.; Melkonian, R.; Arko, R.A.; Weissel, V.; Ferrini, A.; Goodwillie, F.; Nitsche, J.; Bonczkowski, B and Zemsky, R. 2009, Global Multi-Resolution Topography (GMRT) synthesis data set, Geochemistry Geophysics Geosystems., 10, Q03014, doi:10.1029/2008GC002332.

[43] Kramers, J.D.; Roddick, J.C.M. and Dawson, J.B. 1983, Trace element and isotope studies on veined, metasomatic and "MARID" xenoliths from Bultfontein, South Africa. Earth and Planetary Sciences Letters 65, 90–106.doi.org/10.1016/0012-821X(83)90192-9.

[44] Rybach, L. (1988) Determination of the heat production rate. In: Rybach L, Stegena L, Haenel R (eds) Handbook of terrestrial heat-flow density determination. Kluwer, Dordrecht.

[45] Chiozzi P, Pasquale V, Verdoya, M. (2002) Heat from radioactive elements in young volcanic rocks by gamma Ray spectrometry. J Volcan. Geoth. Res. 119:205–214

Journal Pre-proof

Journal Pre-proof

[46] Clauser, C. (2011) Radiogenic Heat Production of Rocks. In: Harsh Gupta (Ed.), Encyclopedia of Solid Earth Geophysics, 2nd ed., Springer, Dordrecht, preprint. DOI: 10.1007/978-90-481-8702-7_74

[47] Wicks, F.J., Whittaker, E.J.W., 1977. Serpentine textures and serpentinization. Can. Mineral. 15, 459–488.

[48] Morandi, N., Felice, G., 1979. Serpentine minerals from veins in serpentinite rocks. Mineral. Mag. 4, 135–140.

[49] Andreani, M., Luquot, L., Gouze, P., Godard, M., Gibert, B., 2009. Experimental study of carbon sequestration reactions controlled by the percolation of CO2-rich brine through peridotites. Environ. Sci. Technol. 43, 1226–1231.

[50] Andreani, M., Mével, C., Boullier, A. M., Escartín, J., 2007. Dynamic control on serpentine crystallization in veins: constraints on hydration processes in oceanic peridotites. Geochem. Geophys. Geosyst. 8, 1–24. https://doi.org/10.1029/2006GC001373.

[51] Fryer, P. (2002) Recent studies of serpentinite occurrences in the oceans: Mantle ocean interactions in the plate tectonic cycle. Chemie Der Erde-Geochemistry, 62, 257-302.

[52] Rudge, J.F., Kelemen, P.B., Spiegelman, M., 2010. A simple model of reaction-induced cracking applied to serpentinization and carbonation of peridotite. Earth Planet. Sci. Lett. 291, 215–227. https://doi.org/10.1016/j.epsl.2010.01.016.

[53] Noort, R. Van, Spiers, C.J., Drury, M.R., Kandianis, M.T., 2013. Peridotite dissolution and carbonation rates at fracture surfaces under conditions relevant for in situ mineralization of CO2. Geochem. Cosmochim. Acta 106, 1–24. https://doi.org/10.1016/j.gca.2012.12.001.

[54] Peuble, S., Andreani, M., Gouze, P., Pollet-Villard, M., Reynard, B., Van de Moortele, B., 2018. Multi-scale characterization of the incipient carbonation of peridotite. Chem. Geol. 476, 150–160. https://doi.org/10.1016/j.chemgeo.2017.11.013.

[55] Andreani, M., Muñoz, M., Marcaillou, C., Delacour, A., 2013. µXANES study of iron redox state in serpentine during oceanic serpentinization. Lithos 178, 70–83. https://doi.org/10.1016/j.lithos.2013.04.008

[55] Scambelluri, M., Müntener, O., Ottolini, L., Pettke, T.T., Vannucci, R., 2004. The fate of B, Cl and Li in the subducted oceanic mantle and in the antigorite breakdown fluids. Earth and Planetary Science Letters 222, 217–234.

[56] Hattori, K.H., Guillot, S., 2007. Geochemical character of serpentinites associated with high- to ultrahigh-pressure metamorphic rocks in the Alps, Cuba, and the Himalayas: recycling of elements in subduction zones. Geochemistry Geophysics Geosystems 8 (9). doi:10.1029/2007GC001594.

[57] Tenthorey, E., Hermann, J., 2004. Composition of fluids during serpentinite breakdown in subduction zones: evidence for limited boron mobility. Geology 32 (10), 865–868.

[58] Wass, S.Y. and Roger, N.W. (1980) Mantle metasomatism—precursor to continental alkaline volcanism. Geochimica et. Cosmochimica Acta 44, 1811–1823. doi.org/10.1016/0016-7037(80)90230-6

[59] Bailey, E.H., Ragnarsdottir, K.V., 1994. Uranium and thorium solubilities in subduction zone fluids. Earth and Planetary Science Letters 124, 119–129.

[60] Olivier, N., Boyet, M., 2006. Rare earth and trace elements of microbialites in Upper Jurassic coral- and sponge-microbialite reefs. Chemical Geology 230,105–123.

[61] Shen, G.T., Dunbar, R.B., 1995. Environmental controls on uranium in reef corals. Geochimica et Cosmochimica Acta 59 (10), 2009–2024.

[62] Turekian, K.K., Wedepohl, H., 1961. Distribution of the elements in some major units of the Earth's crust. Geological Society of America Bulletin 72, 175–192.

[63] Smedley, P.L., Kinniburgh, D.G., 2002. A review of the source, behaviour and distribution of arsenic in natural waters. Applied Geochemistry 17, 517–568.

[64] Takahashi, Y., Minamikawa, R., Hattori, K.H., Kurishima, K., Nihou, N., Yuita, K., 2004. Arsenic behaviour in paddy fields during the cycle of flooded and non-flooded periods. Environmental Sciences Technology 38, 1038–1044.

[65] Birch, F., Roy, R.F., Decker, E.R (1968) Heat flow and thermal history in New England and New York. In: Zen, E., White,mW.S., Hadley, J.B., Thompson, J.B. Eds.., Studies of Appalachian Geology: Northern and Maritime. Interscience, New York, pp. 437–451.

[66] Roy, R. F., Blackwell, D. D., Birch, F. (1968) Heat generation of plutonic rocks and continental heat flow provinces, Earth Planet. Sci. Lett., 5, 1-12.

[67] Stein, C.A. (1995) Heat Flow of the Earth. in A Handbook of Physical Constants AGU Reference Shelf. 376 pages. https://doi.org/10.1029/RF001p0144

[68] Hasterok, D., Chapman, D. (2011) Heat production and geotherms for the continental lithosphere. Earth and Planetary Science Letters 307, 59e70. https://doi.org/10.1016/j.epsl.2011.04.034.

[69] McDonough, W.F and Sun, S.-s 1995. The composition of the Earth. Chemical Geology, 120, 223-253. SSDI 00092541(94)00140-5

[70] Clark, S. P. and Ringwood, A. E. (1964) Density distribution and constitution of the mantle, Rev. Geophys., 2, 35-88.

[71] Hasterok, D., Webb, J., 2017. On the radiogenic heat production of igneous rocks. Geoscience Frontiers 8, 919e940. doi.org/10.1016/j.gsf.2017.03.006.

[72] Hasterok, D., Gard, M. and Web, J. (2018). On the radiogenic heat production of metamorphic, igneous, and sedimentary rocks. Geoscience Frontiers 9/6, 1777-1794. https://doi.org/10.1016/j.gsf.2017.10.012

[73] Rybach, L. 1976. Radioactive heat production in rocks and its relation to other petrophysical parameters. PAGEOPH 114, 309–317 (1976). https://doi.org/10.1007/BF00878955

[74] Rybach, L. and Cërmák, V. (1982) Radioacive heat generation in rocks. In G. Angenheister (Ed), LAndolt-Börnstein Zahlenwerte and Funkitionen aus Natur wissenschaften und Tecnik, neue Serie, Phyiskalische eigneschaften de Gsteiene. Spring Verlag, Berlin, Heidelberg and New York, v*1a, 353-371

[75] Rudnick, R.L., McDonough, W.F., O'Connell RJ. (1998) Thermal structure, thickness and composition of continental lithosphere. Chem. Geol. 145:395–411.

Journal Pre-proof

[76] Jaupart, C. and Mareschal, J.-C. (2007) Heat flow and thermal structure of the lithosphere. In: Shubert, G., Watts, A. (Eds.), Treatise on Geophysics: Crust and Lithospheric Dynamics. Vol. 6. Elsevier, Ch. 5, pp. 217–251.

[77] Russell, J. K., Dipple G.M. and Kopylova, M.G. (2001) Heat production and heat flow in the mantle lithosphere, Slave craton, Canada. Physics of the Earth and Planetary Interiors 123: 27–44.

[78] Davies, F.D (1980) Review of oceanic and global heat flow estimates Reviews of Geophysics doi.org/10.1029/RG018i003p00718

[79] Jaupart C., Labrosse S. and Mareschal, J.-C. (2007) Temperatures, Heat and Energy in the Mantle of the Earth. In: Shubert, G., Watts, A. (Eds.), Treatise on Geophysics: Crust and Lithospheric Dynamics. Vol. 7. Elsevier, Ch. 6, pp. 254-303.

[80] Pasquale, Massimo and Chiozzi, (2014) Geothermics Heat Flow in the Lithosphere. Springer Briefs in Earth Sciences DOI 10.1007/978-3-319-02511-7

[81] Jessop A.M., 1990: Thermal geophysics, Elsevier, Amsterdam, 316 pp.

[82] Bonatti, E and Michel, P.J. (1989) Mantle peridotites from continental rifts to ocean basins to subduction zones. Earth and Planetary Science Letters, 91/ 3–4, 1989, 297-311. https://doi.org/10.1016/0012-821X(89)90005-8

[83] Bonatti, E., 1990. Subcontinental mantle exposed in the Atlantic Ocean on St. Peter-Paul islets. Nature 345, pp. 800-802.

[84] Bonatti, E. Brunelli, D., Fabretti, P., Ligi, M. Portaro, R.A., Seyler, M. (2001) Steady-state creation of crust-free lithosphere at cold spots in mid-ocean ridges. Geology 29 (11): 979–982. doi: https://doi.org/10.1130/0091-7613(2001)029<0979:SSCOCF>2.0.CO;2

[85] Bonatti, E., and Honnorez, J. (1976) Sections of the Earth's crust in the equatorial Atlantic: Journal of Geophysical Research, v. 81, p. 4104–4116.

[86] Bonatti, E., Seyler, M., Sushevskaya, N. (1993). A cold sub-oceanic mantle belt at the Earth's equator. Science 261, 315–320. Number: ISI: A1993LM67800026.

647 Table 1: Statistical synthesis of HPE by whole-rock chemical analysis and density results from the
648 peridotite and kaersutite mylonites rocks of St. Peter and St. Paul archipelago. Max: Maximum; Min:
649 Minimum; μ: Geometric mean; σ: Standard deviation.
650

Islet	Rock type		U (ppm)	Th (ppm)	K (%)	Density (kg/m^3)
Belmonte	Peridotite mylonite serpentinized	Max	0.30	0.70	0.15	3339.00
		Min	0.20	0.28	0.11	3138.00
		μ	0.24	0.40	0.13	3274.95
	(n: 30)	σ	0.04	0.13	0.01	67.86
	Peridotite mylonite serpentinized	Max	0.29	0.67	0.17	2453.00
		Min	0.20	0.29	0.12	2014.00
		μ	0.25	0.48	0.14	2160.47
		σ	0.03	0.12	0.02	159.25
	Peridotites mylonite halmyrolized	Max	0.29	0.67	0.17	2453.00
		Min	0.20	0.29	0.12	2014.00
		μ	0.25	0.48	0.14	2160.47
		σ	0.03	0.12	0.02	159.25
Northeast	Peridotite mylonite serpentinized	Max	1.37	0.70	0.20	3285.00
		Min	1.00	0.22	0.11	2985.00
		μ	1.19	0.29	0.13	3133.75
		σ	0.11	0.15	0.03	99.15
Northwest	Peridotite mylonite serpentinized	Max	1.24	0.29	0.17	3120.00
		Min	1.21	0.28	0.12	3000.00
		μ	1.23	0.28	0.14	3045.97
		σ	0.01	0.01	0.02	43.16
South	Peridotite mylonite serpentinized	Max	1.24	0.29	0.17	3120.00
		Min	1.21	0.28	0.12	3000.00
		μ	1.23	0.28	0.14	3045.97
		σ	0.01	0.01	0.02	43.16
Coutinho	Peridotite mylonite serpentinized	Max	2.15	0.40	0.39	3016.00
		Min	2.00	0.37	0.26	3016.00
		μ	2.08	0.38	0.32	3016.00
		σ	0.06	0.01	0.06	0.00
Southeast	Peridotite mylonite serpentinized	Max	2.64	0.62	0.16	3254.00
		Min	1.20	0.27	0.10	2056.00
		μ	1.70	0.37	0.13	2444.16
		σ	0.48	0.11	0.02	432.65
	Layered Kaersutite-peridotite	Max	0.34	0.50	0.44	3247.00
		Min	0.10	0.30	0.10	2547.00
		μ	0.21	0.37	0.23	2907.00
		σ	0.07	0.07	0.11	211.12
	Kaersutite mylonite (n : 16)	Max	0.34	0.50	0.44	3247.00
		Min	0.10	0.30	0.10	2547.00
		μ	0.21	0.37	0.23	2907.00
		σ	0.07	0.07	0.11	211.12

Journal Pre-proof

651 Table 2: Statistical synthesis of HPE by *is*GRS and density results from peridotite and kaersutite
652 mylonites rocks of St. Peter and St. Paul archipelago. AE: Activity equivalent; Max: Maximum;
653 Min: Minimum; μ: Geometric mean; σ: Standard deviation.
654

Rock type		**U**	**Th**	**K**	**Mean Density**
		(AE ppm)	**(AE ppm)**	**(AE %)**	**kg/m³**
Peridotite mylonite (n: 50)	Max	0.90	0.81	0.40	3281.33
	Min	0.20	0.10	0.10	
	μ	0.37	0.47	0.14	
	σ	0.11	0.18	0.09	
Peridotite mylonite serpentinized (n: 200)	Max	3.66	1.10	0.40	2884.61
	Min	2.00	0.10	0.10	
	μ	2.55	0.31	0.12	
	σ	0.29	0.22	0.07	
Layered kaersutite-peridotite mylonite (n:50)	Max	0.88	0.60	0.40	2890.63
	Min	0.45	0.20	0.10	
	μ	0.66	0.35	0.15	
	σ	0.10	0.17	0.10	

655
656
657
658
659
660

Journal Pre-proof

661 Table 3: Linear regression coefficients of ICP-MS versus *is*GRS values of U and Th given in Table 1.

Rock type	**Correlation**	**Intercept**	**Slop**	R^2
Peridotite mylonite	U_{ICP-MS} x U_{isGRS}	0.1195	0.9983	0.9979
	Th_{ICP-MS} x Th_{isGRS}	0.1227	0.9787	0.9954
Peridotite mylonite serpentinized	U_{ICP-MS} x U_{isGRS}	1.0995	0.9519	0.9915
	Th_{ICP-MS} x Th_{isGRS}	0.2047	1.0012	0.9925
Layered kaersutite-Peridotite mylonite	U_{ICP-MS} x U_{isGRS}	0.2960	1.6797	0.9990
	Th_{ICP-MS} x Th_{isGRS}	-0.0944	1.3425	0.9989
Kaersutite mylonite	U_{ICP-MS} x U_{isGRS}	0.3408	2.0021	0.9991
	Th_{ICP-MS} x Th_{isGRS}	0.0873	1.0741	0.9916

662

663 Table 4: Statistical synthesis of surface RHP (A_0: μWm^3) results from mylonite rocks of SPSPA. Max:
664 Maximum; Min: Minimum; GM: Geometric Mean; Med: Median; SD: Standard Deviation.
665

Radioactive Heat Production	**Max**	**Min**	**GM**	**Med**	**SD**
A_0: $\mu W/m^3$(Chemical whole-rock)	0.68	0.08	0.25	0.21	0.15
A_0: $\mu W/m^3$ (*is*GRS)	0.48	0.08	0.19	0.19	0.50

666

667

668

669

670

671

672

673

Journal Pre-proof

Journal Pre-proof

674 Table 5 : Average trace and major elements of rocks from SPSPA. *: below limite detection; LOI: Lost on ignition.

	Unserpentinized peridotite mylonite (n:14) **(LOI <1%)**	**Serpentinized peridotite mylonite (n: 28)** **(1% > LOI <5%)**	**Serpentinized peridotite mylonite (n: 14)** **(5% > LOI <15%)**	**Layered Kaersutite-Peridotite mylonite (n: 13)** **(LOI = 2,43%)**	**Kaersutite mylonite (n: 16)** **(LOI = 1,40 %)**
Cs	*	*	*0.14*	*0.11*	*0.17*
Rb	*0.86*	*1.96*	*0.32*	*2.68*	*10.13*
Ba	*16.29*	*17.45*	*11.40*	*185.15*	*2270.06*
Th	*0.35*	*0.33*	*0.33*	*0.39*	*0.54*
U	*0.13*	*0.17*	*1.71*	*0.21*	*0.13*
Nb	*2.35*	*2.93*	*0.96*	*9.23*	*1.58*
Ta	*0.14*	*0.15*	*0.14*	*0.59*	*0.10*
La	*3.80*	*2.76*	*2.16*	*8.98*	*19.14*
Ce	*6.17*	*4.98*	*3.07*	*18.96*	*42.00*
Pr	*0.40*	*0.30*	*0.27*	*2.41*	*5.20*

Journal Pre-proof

Pb	*6.28*	*5.62*	*9.17*	*5.46*	*27.69*
Nd	*1.10*	*0.82*	*0.75*	*9.08*	*21.55*
Sr	*27.82*	*20.92*	*149.07*	*199.28*	*888.31*
Sm	*0.22*	*0.19*	*0.17*	*1.84*	*5.34*
Zr	*43.31*	*36.57*	*31.67*	*46.78*	*62.84*
Hf	*0.84*	*0.66*	*0.23*	*1.22*	*1.83*
Eu	*0.07*	*0.06*	*0.06*	*0.58*	*1.66*
Gd	*0.21*	*0.20*	*0.19*	*1.68*	*4.64*
Tb	*0.03*	*0.03*	*0.03*	*0.24*	*0.67*
Dy	*0.21*	*0.21*	*0.19*	*1.13*	*3.40*
Ho	*0.05*	*0.05*	*0.04*	*0.22*	*0.62*
Er	*0.13*	*0.13*	*0.12*	*0.51*	*1.53*
Y	*1.39*	*1.24*	*1.53*	*5.53*	*19.89*
Tm	*0.02*	*0.02*	*0.02*	*0.07*	*0.21*
Yb	*0.14*	*0.14*	*0.13*	*0.44*	*1.15*

Journal Pre-proof

Journal Pre-proof

Lu	*0.03*	*0.03*	*0.02*	*0.07*	*0.16*
Ca %	*0.03*	*0.03*	*0.09*	0.071	0.210
Si %	*0.71*	*0.71*	*0.61*	0.697	0.643

675

Journal Pre-proof

676 Table 6: Statistical synthesis of RHF (q_s: $\mu W/m^2s$) results from mylonite rocks of SPSPA.
677 Max: maximum; Min: Minimum; GM: Geometric mean; MED: Median; SD: Standard
678 Deviation. *is*GRS: in situ gamma ray spectrometry.

679

Surface Heat Flow	Max	Min	GM	MED	SD
Chemical whole-rock q_s: $\mu W/m^2s$	56.4	47.3	50.4	50.1	2.31
*is*GRS q_s: $\mu W/m^2s$	53.3	47.4	59.0	48.2	0.82

680

681

682

683

684

685

686

687

688

689

690

691

692

693

694

Journal Pre-proof

695 **FIGURE'S LEGEND**

696 Figure 1: Location of St. Peter and St. Paul Archipelago, Equatorial Atlantic, Brazil. Figure
697 made with GeoMapApp (www.geomapapp.org) [42].
698
699 Figure 2: Geologic map of St. Peter and St. Paul Archipelago, Equatorial Atlantic, Brazil.
700 Color for Geologic Maps according to the U.S. Geological Survey
701 (https://mrdata.usgs.gov/catalog/lithclass-color.php). Based from [31, 39].
702
703 Figure 3: Hand samples from St. Peter and St. Paul archipelago (Equatorial Atlantic, Brazil):
704 A) Peridotite mylonite; B) Kaersutite mylonite with white carbonate veins; C)
705 Serpentinized peridotite mylonite: C1- Superficial crust sample without serpentine due to
706 the sea-water erosion; C2- Inner surface of C1, D) Layered Kaersutite-Peridotite mylonite:
707 D1- Superficial crust sample, D2- Inner surface of D1.
708
709 Figure 4: Sampling: A) Rock sample location (n: 106); B) Radiometric measurement
710 location (n: 300).
711
712 Figure 5: Comparison among ICP-MS and *is*GRS of uranium and thorium date of peridotite
713 and kaersutite mylonites rocks from SPSPA, Equatorial Atlantic, Brazil.
714
715 Figure 6: Kriging surface color map of surface HPE by whole-rock chemical of peridotite
716 and kaersutite mylonite rocks from SPSPA: A) Uranium (AE-ppm); B) Thorium (AE-ppm); C)
717 Potassium (AE-%). White line: geological contact.
718
719 Figure 7: Kriging surface color map of surface HPE by *is*GRS of peridotite mylonites rocks
720 from St. Peter and St. Paul archipelago (Equatorial Atlantic, Brazil): A) Disintegration
721 (Bq/sec); B) Uranium (AE-ppm);; C) Thorium (AE-ppm);; D) Potassium (AE-%);. White line:
722 geological contact.
723
724 Figure 8: Kriging surface color map of SRHP (A_0) of mylonite rocks from SPSPA obtained by
725 whole-rock chemical analysis (A) and by in situ gamma radiation spectrometry (B). White
726 line: geological contact.
727
728 Figure 9: Primitive Mantle normalized spider-diagram [69] for A) Peridotite mylonite rocks
729 from SPSPA; B) Normalized concentrations of fluid-mobile and fluid-immobile elements in
730 peridotite mylonite from SPSPA. Fluid-mobile elements refer to those with high solubilities
731 in aqueous fluids, to clarify the diagram Fluid-immobile elements are listed in order of
732 compatibility with mantle minerals during partial melting.
733
734 Figure 10: Oceanic lithosphere and continental shield model, assuming a constant flux at
735 200 km depth. The heat flow at different levels is indicated by black thick arrows. Based
736 on [23]
737

Journal Pre-proof

738 Figure 11: Kriging surface color map of surface radiogenic heat flow (q_s: μWm^2s) of
739 mylonites rocks from SPSPA obtained by (A) Whole-rock chemical analysis and (B) In situ
740 gamma radiation spectrometry. White line: geological contact.
741
742 Figure 12: Saint Paul transform system, Equatorial Atlantic. Thick red line: ridge axis; dashed
743 red line: Active transform fault; black dashed line: inactive transform fault. Based [25].

Journal Pre-proof

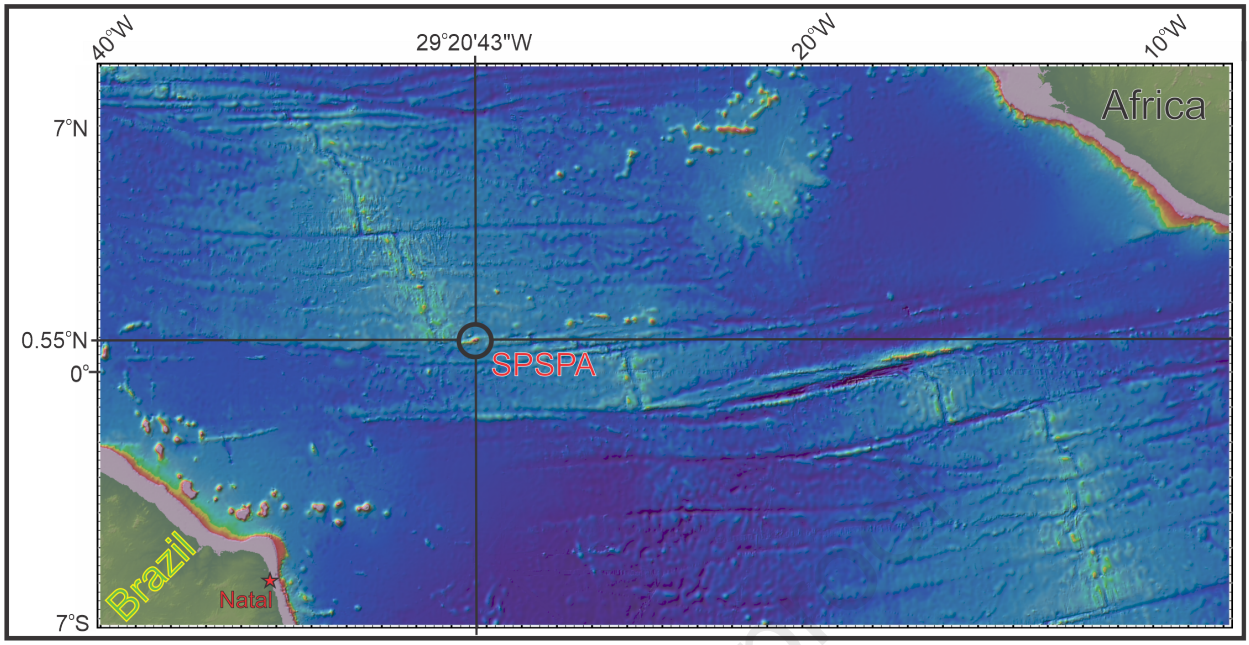

Journal Pre-proof

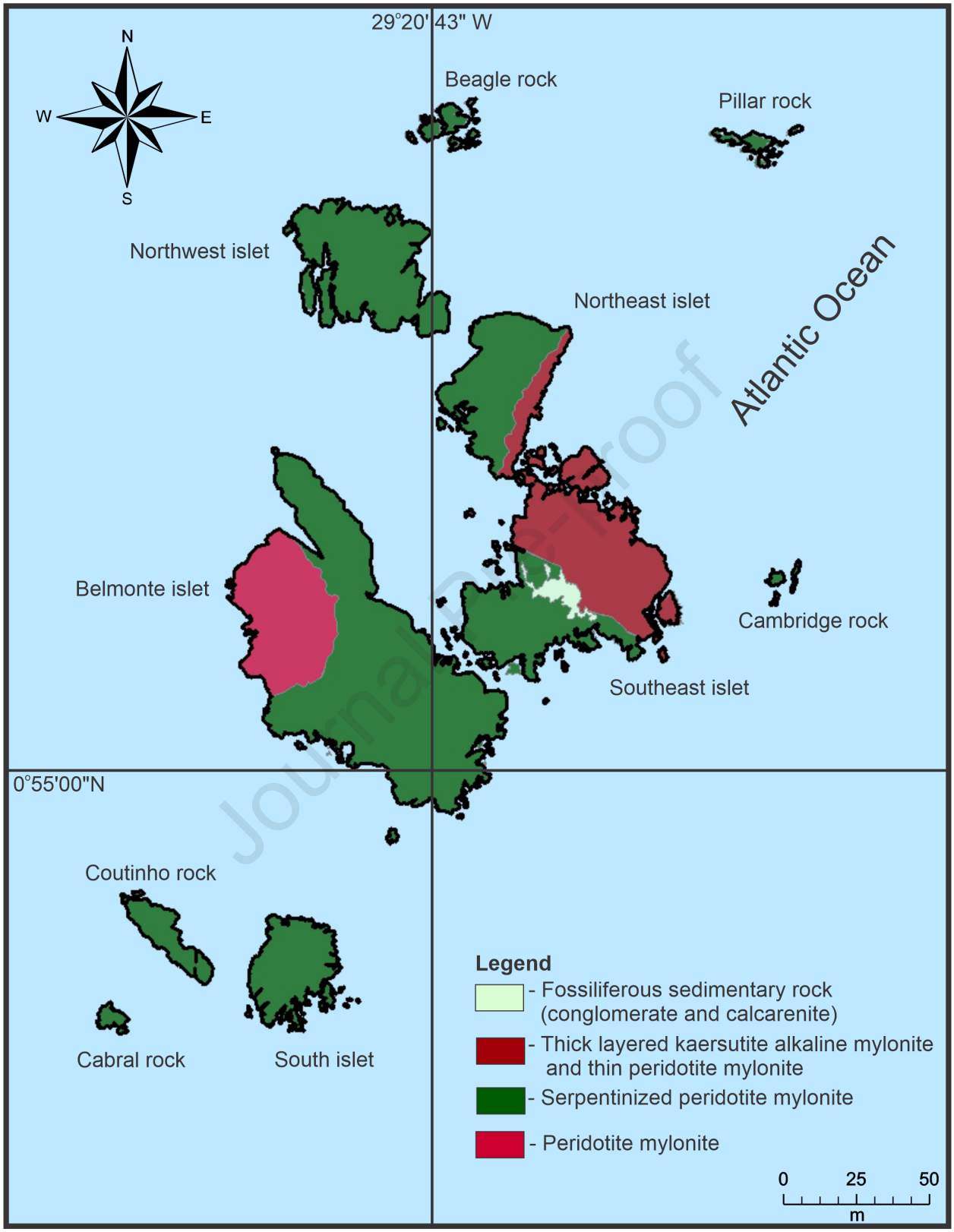

Journal Pre-proof

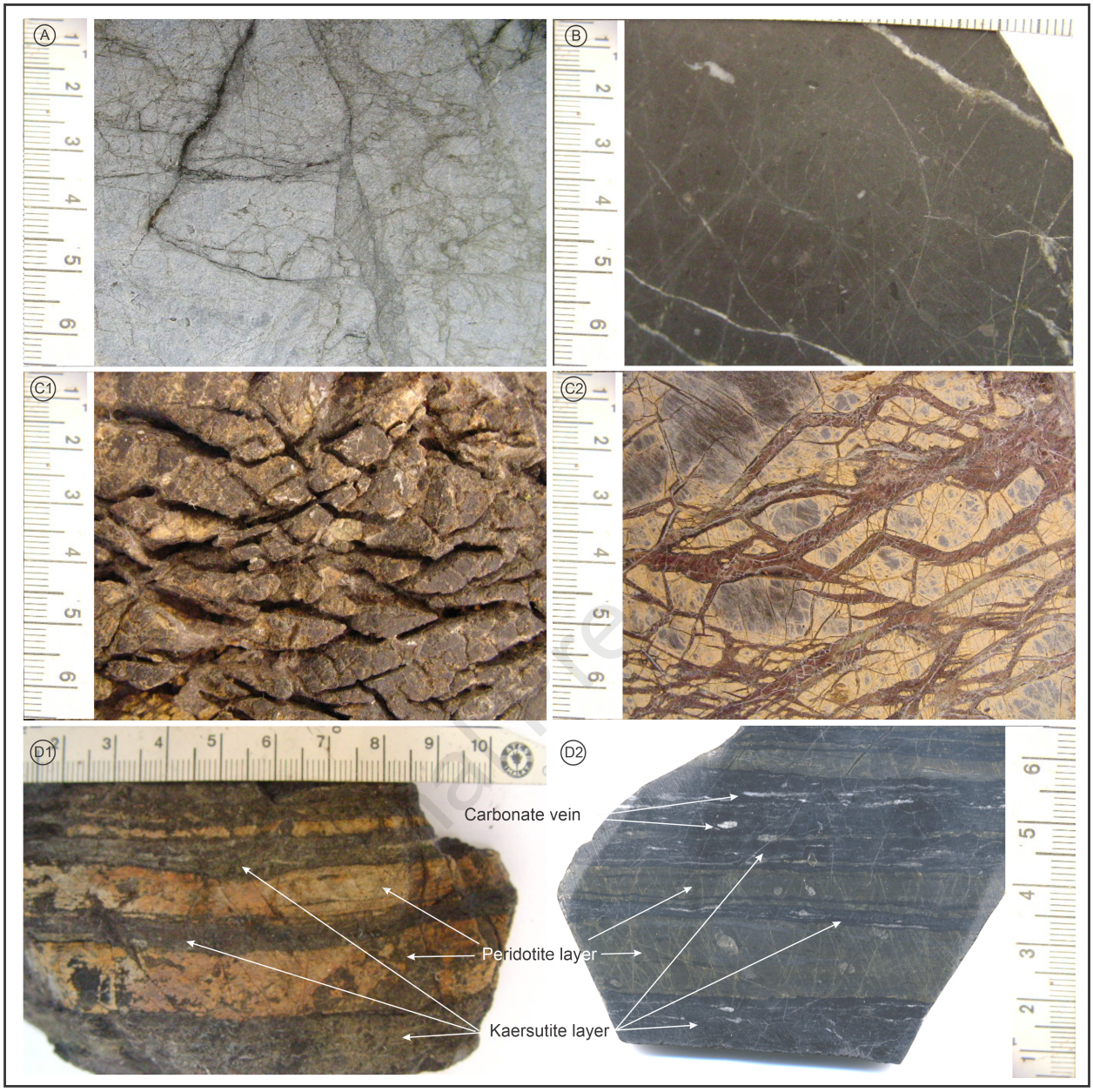
A
B
C1
C2
D1
D2
Carbonate vein
Peridotite layer
Kaersutite layer

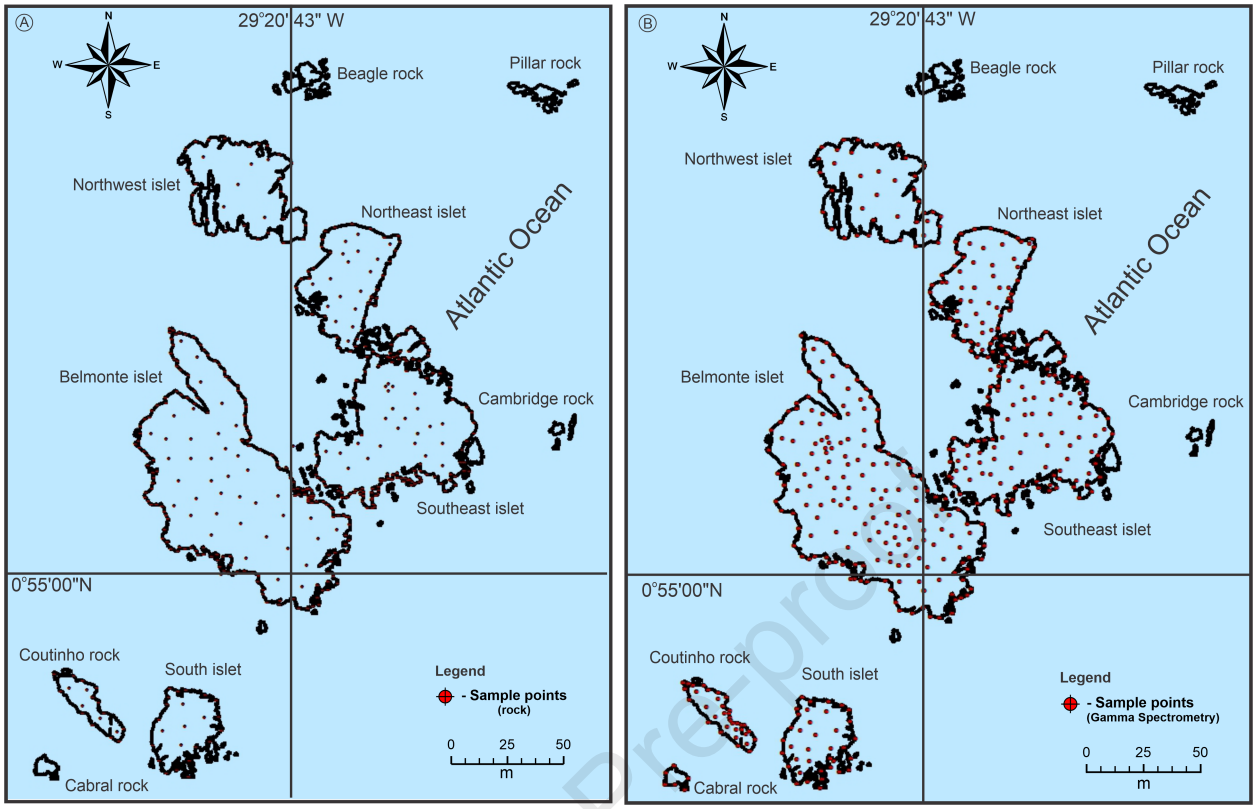

Journal Pre-proof

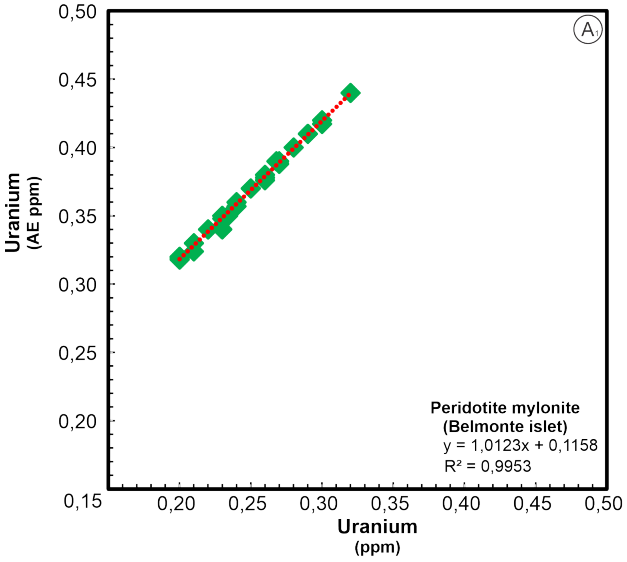

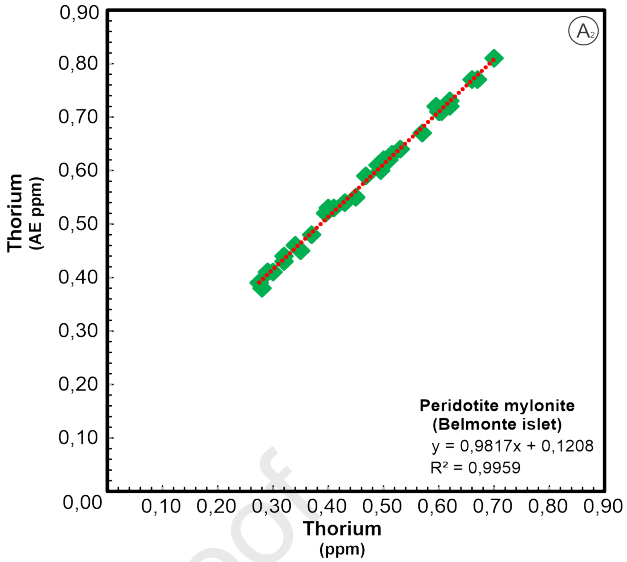

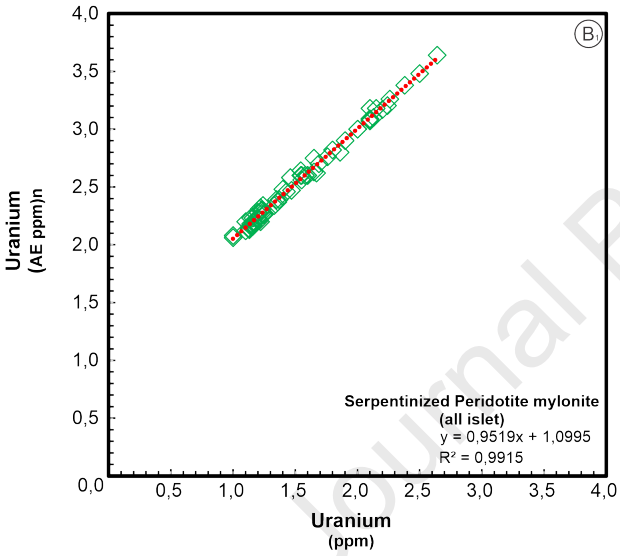

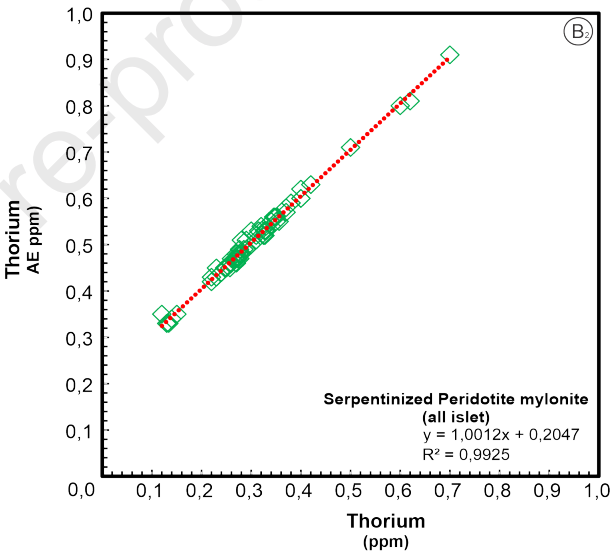

Journal Pre-proof

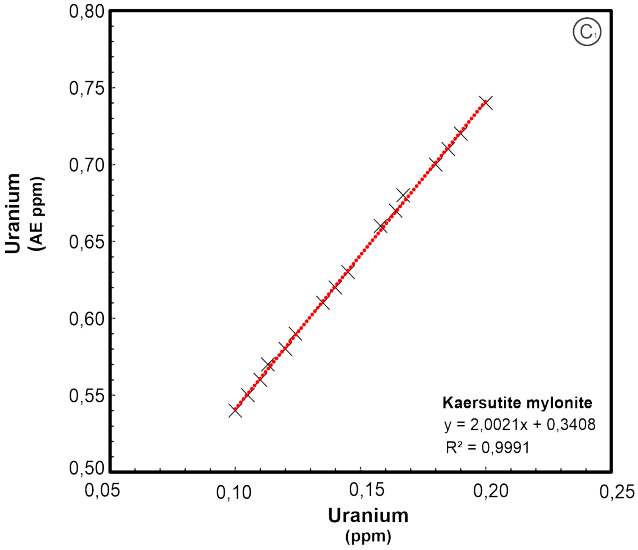

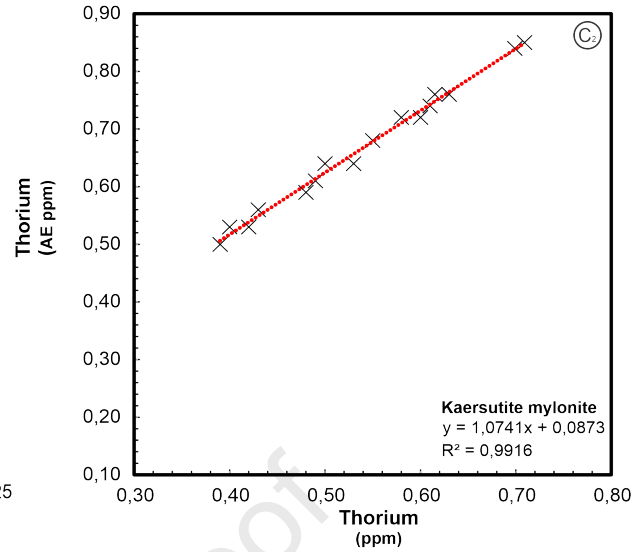

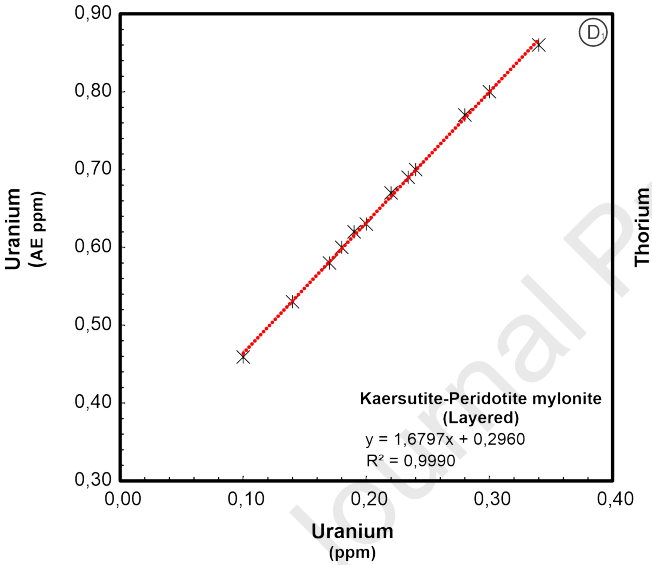

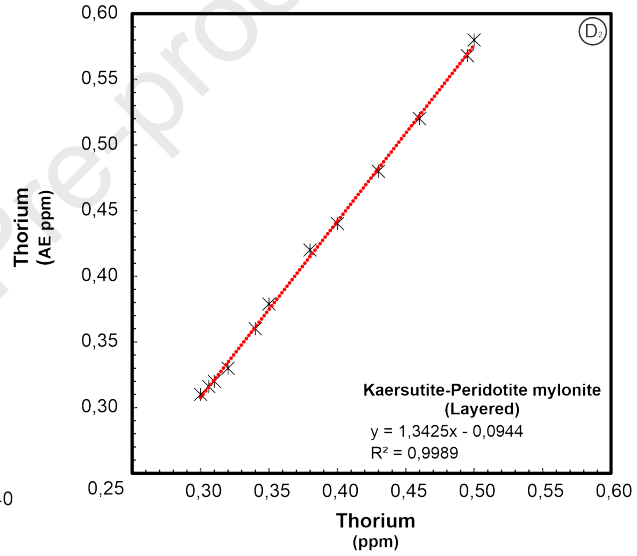

Journal Pre-proof

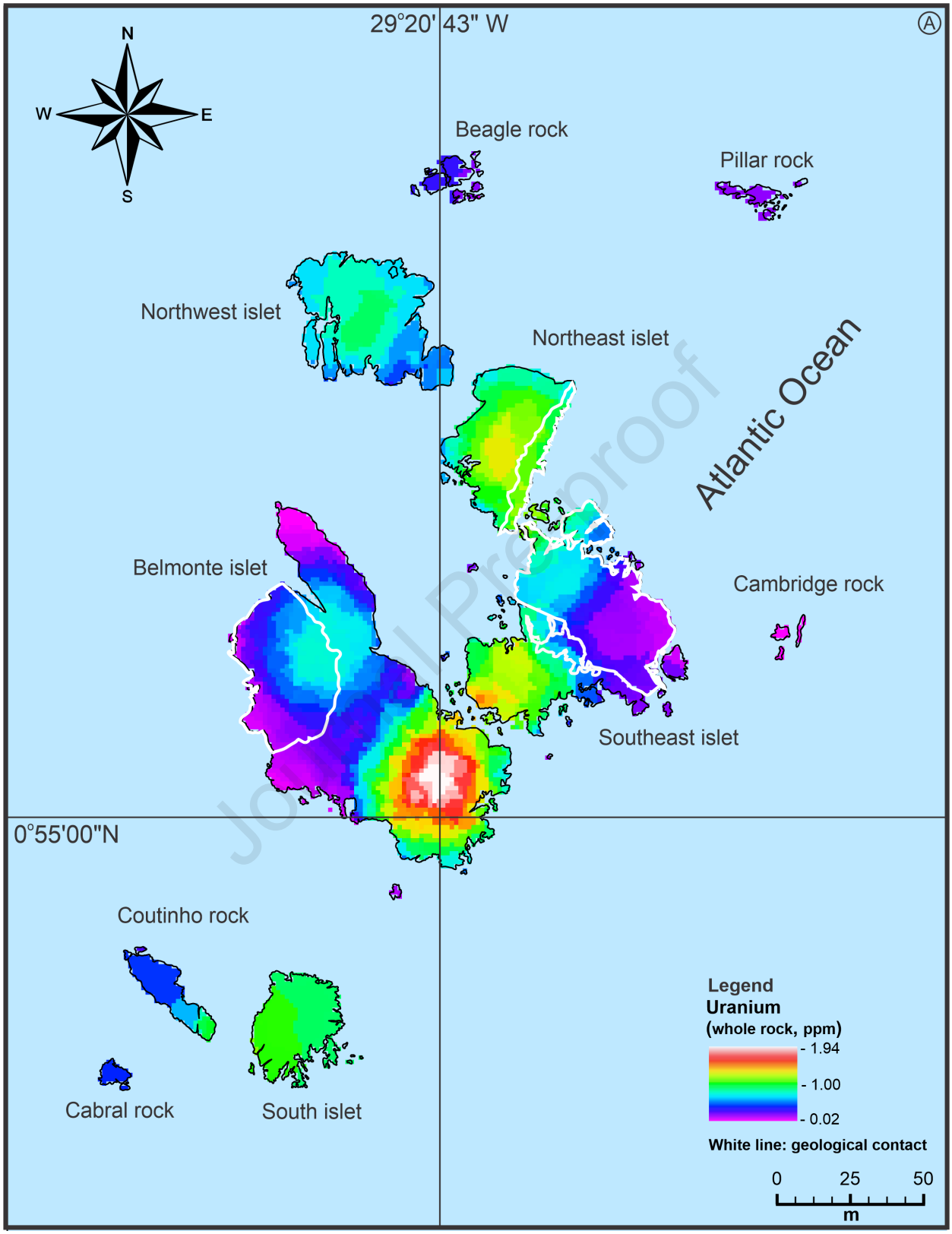

Journal Pre-proof

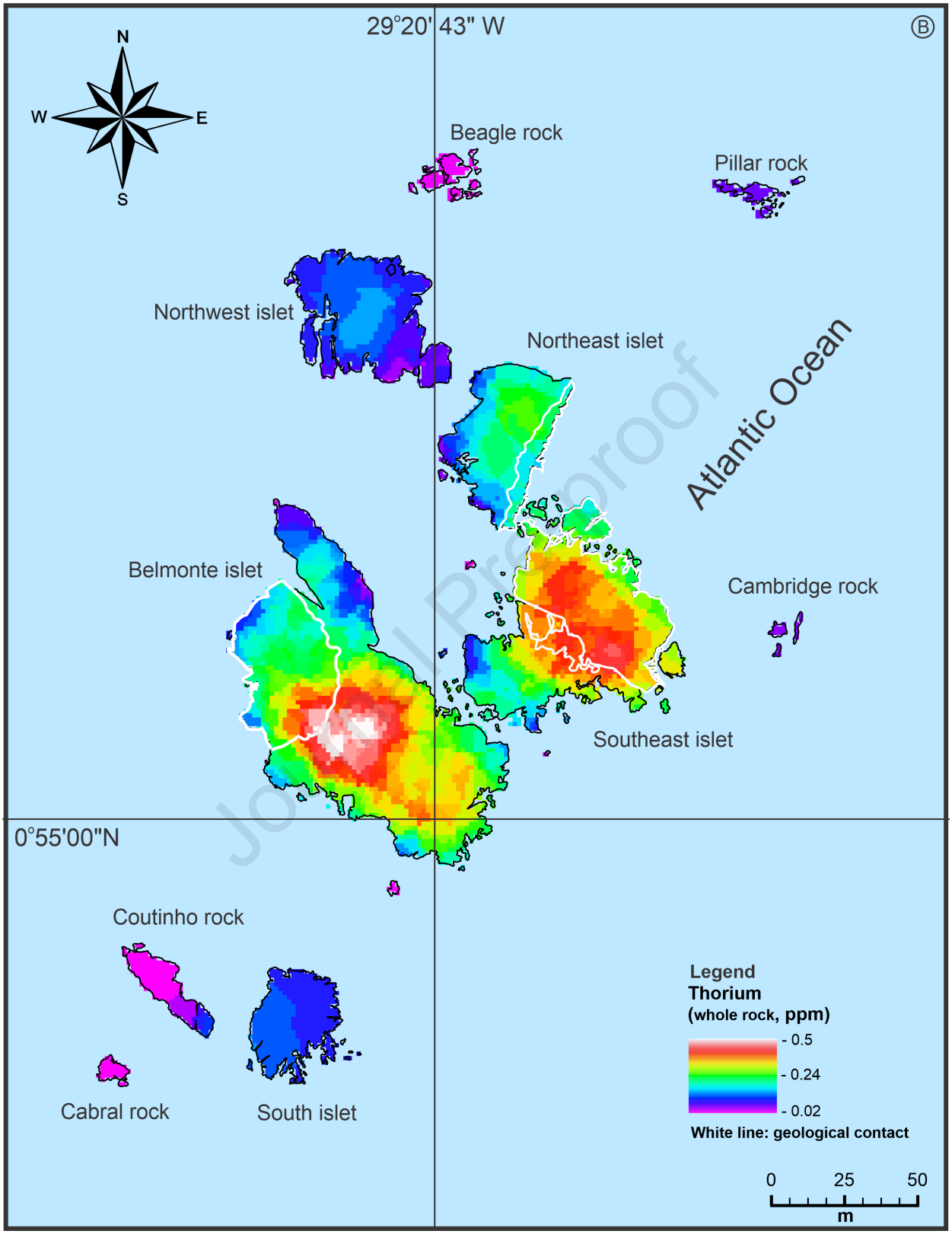

Journal Pre-proof

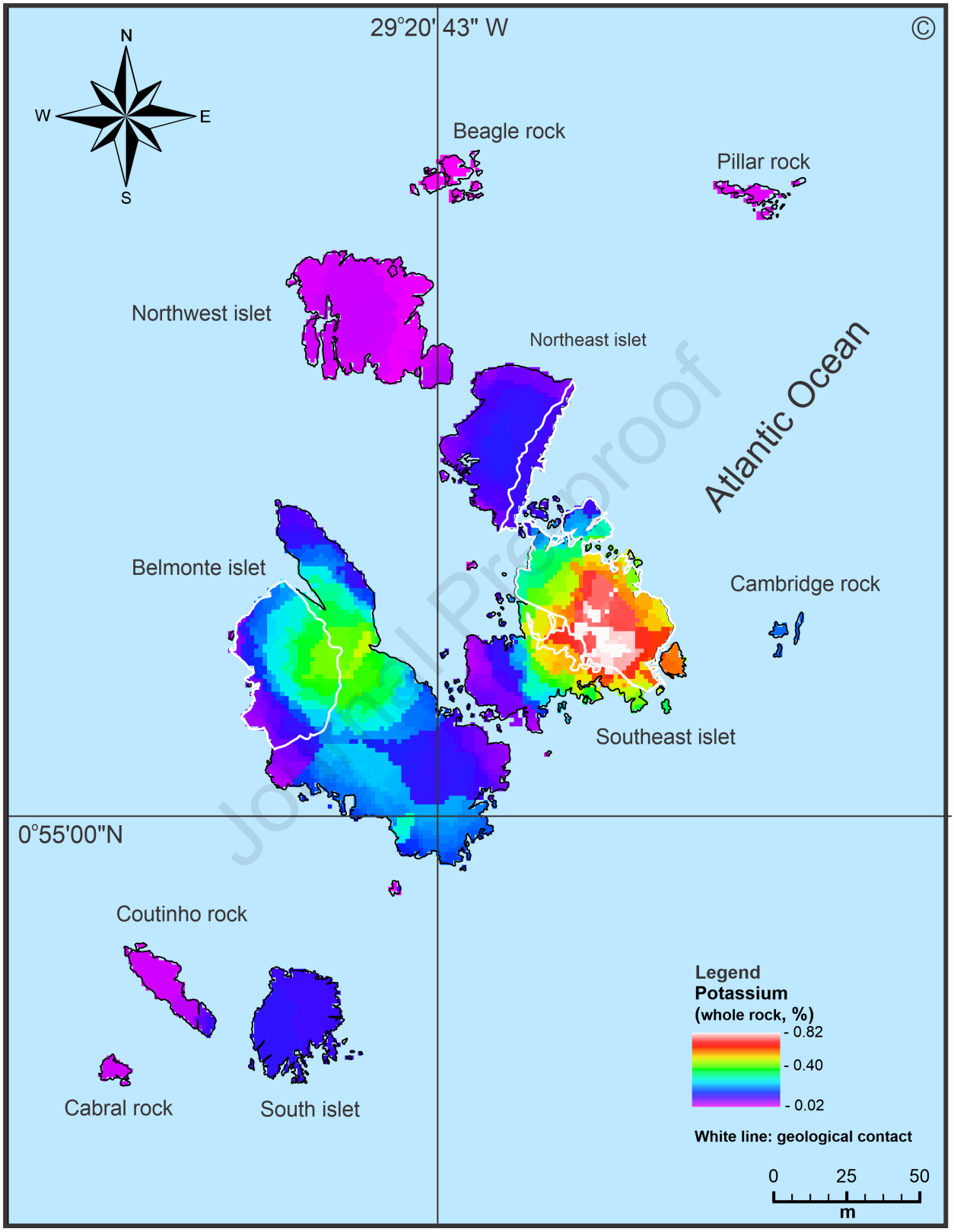

Journal Pre-proof

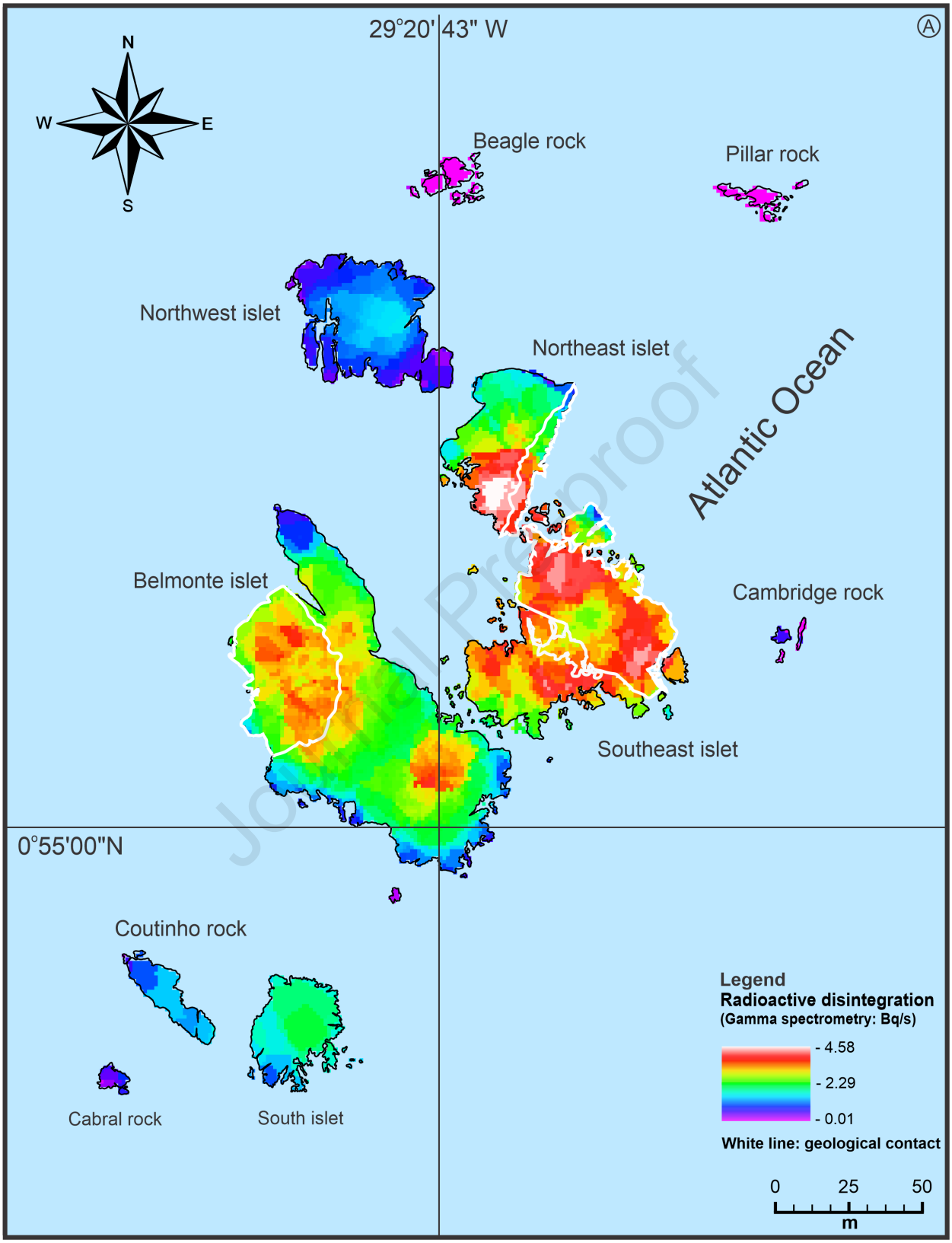

Journal Pre-proof

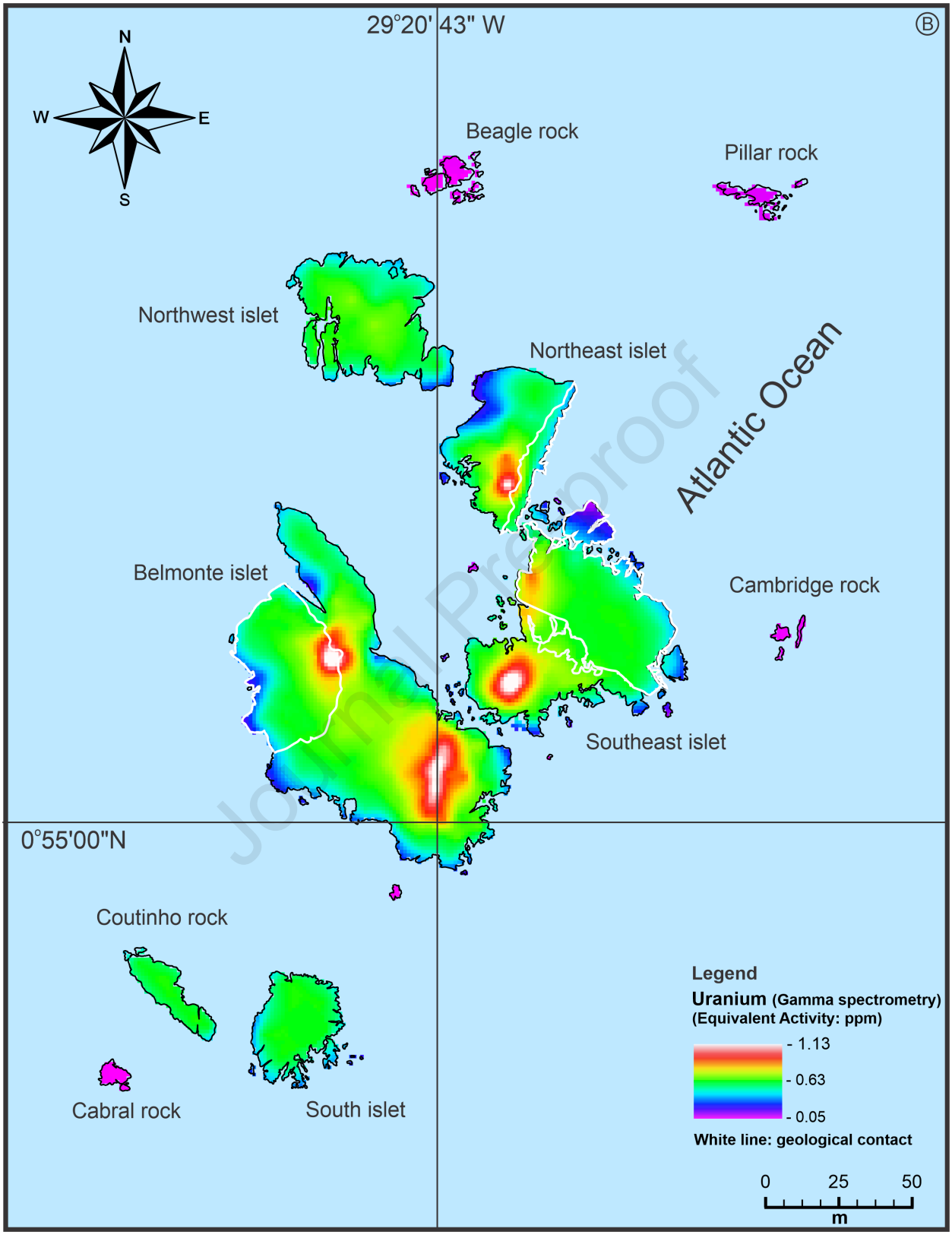

Journal Pre-proof

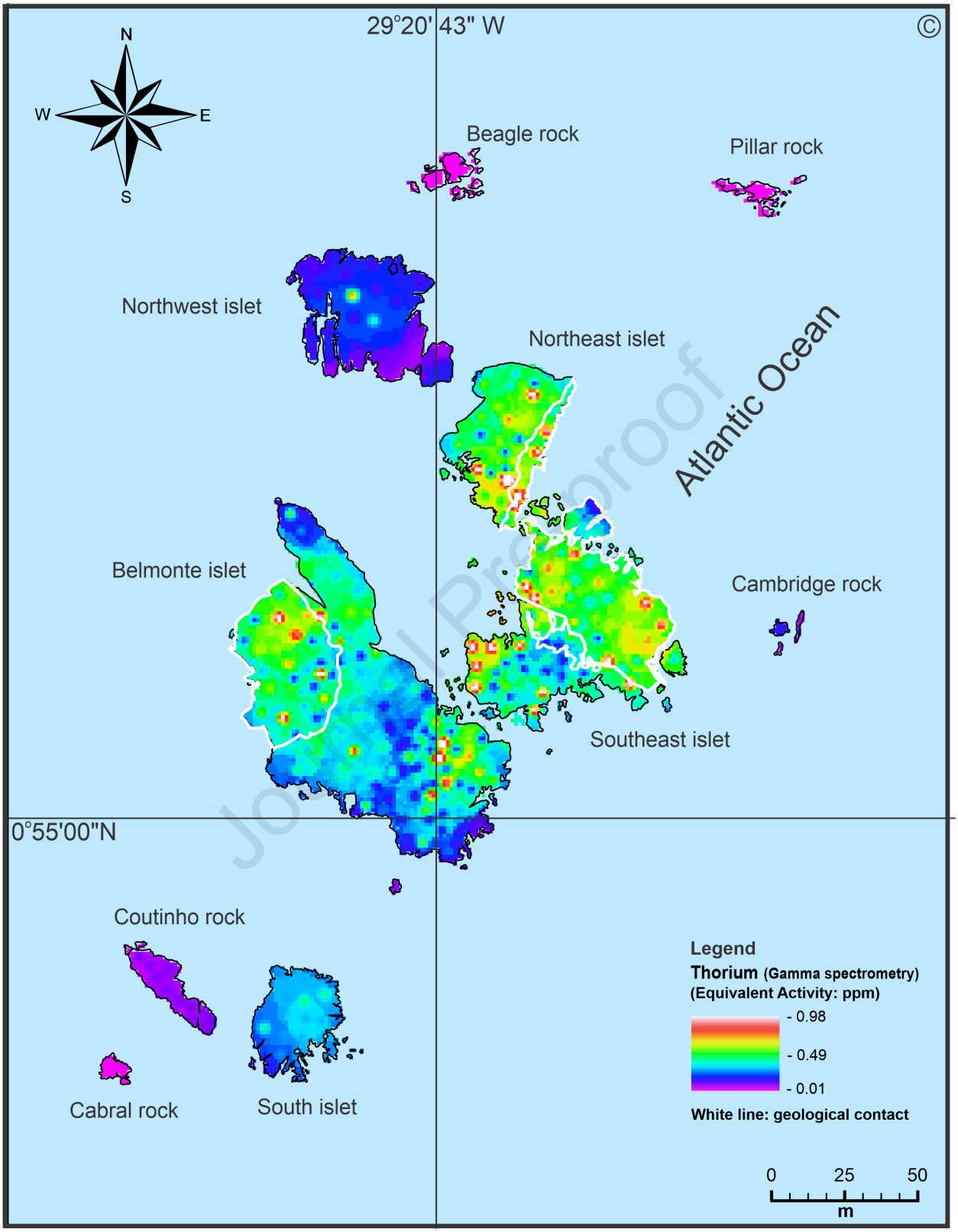

Journal Pre-proof

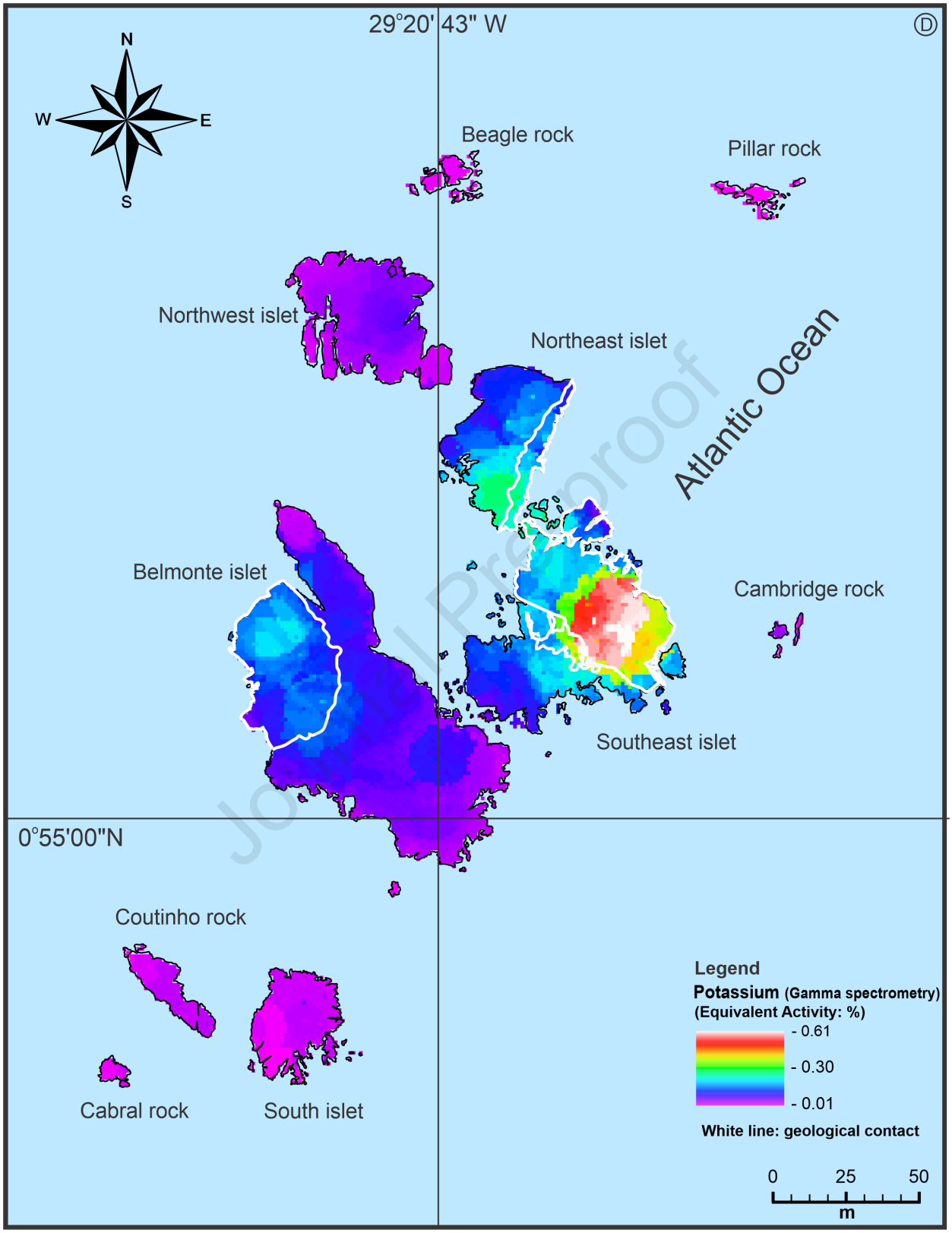

Journal Pre-proof

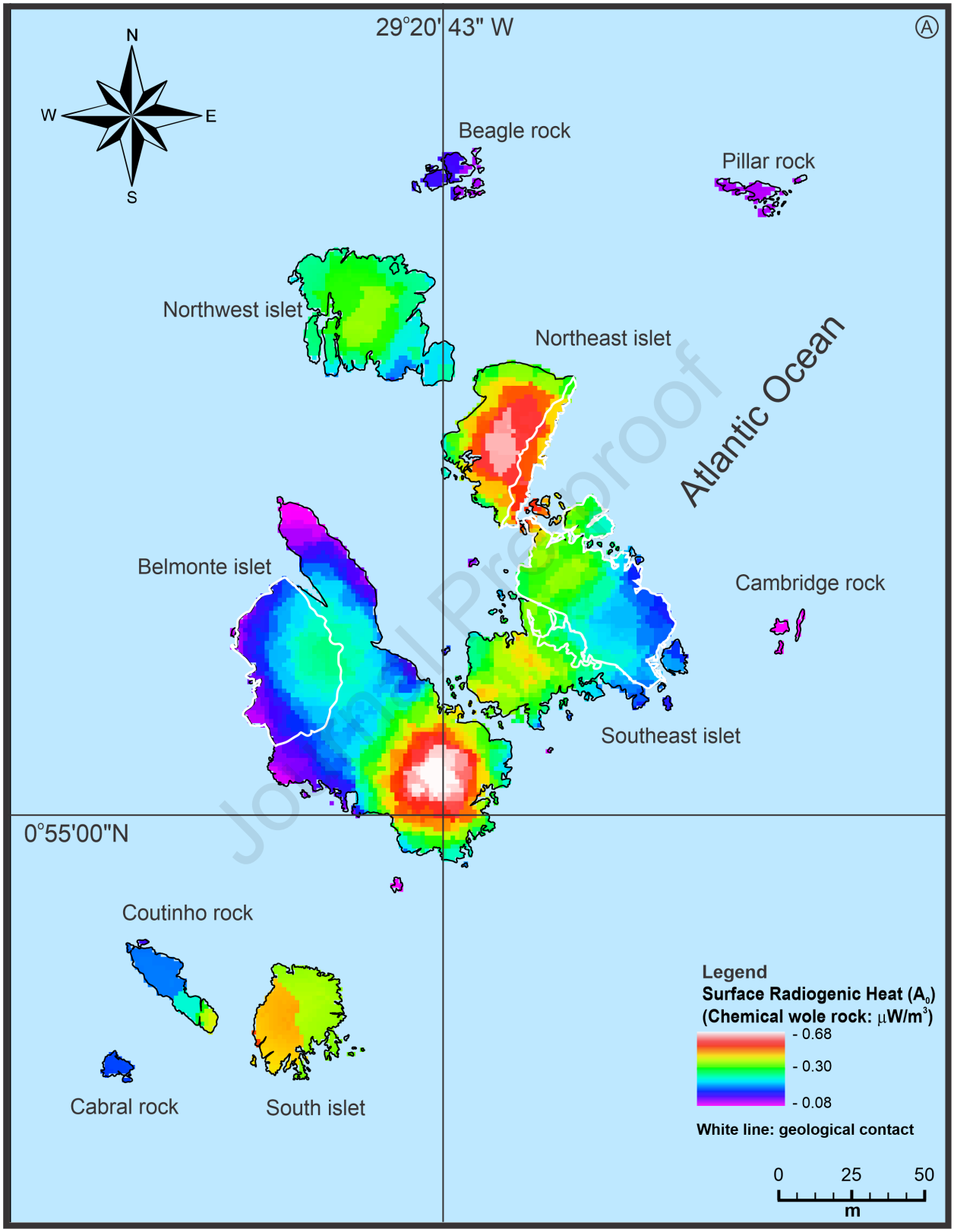

Journal Pre-proof

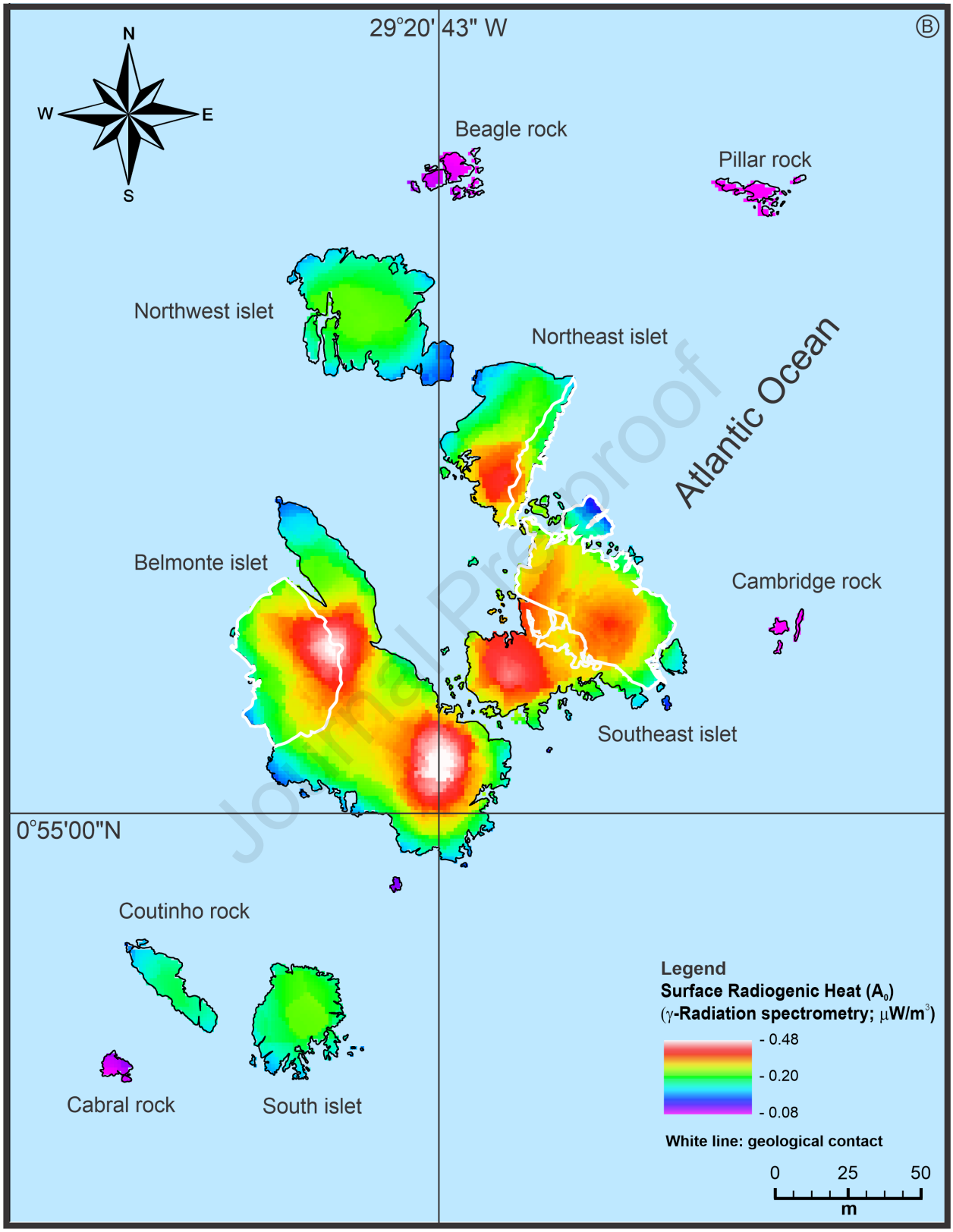

Journal Pre-proof

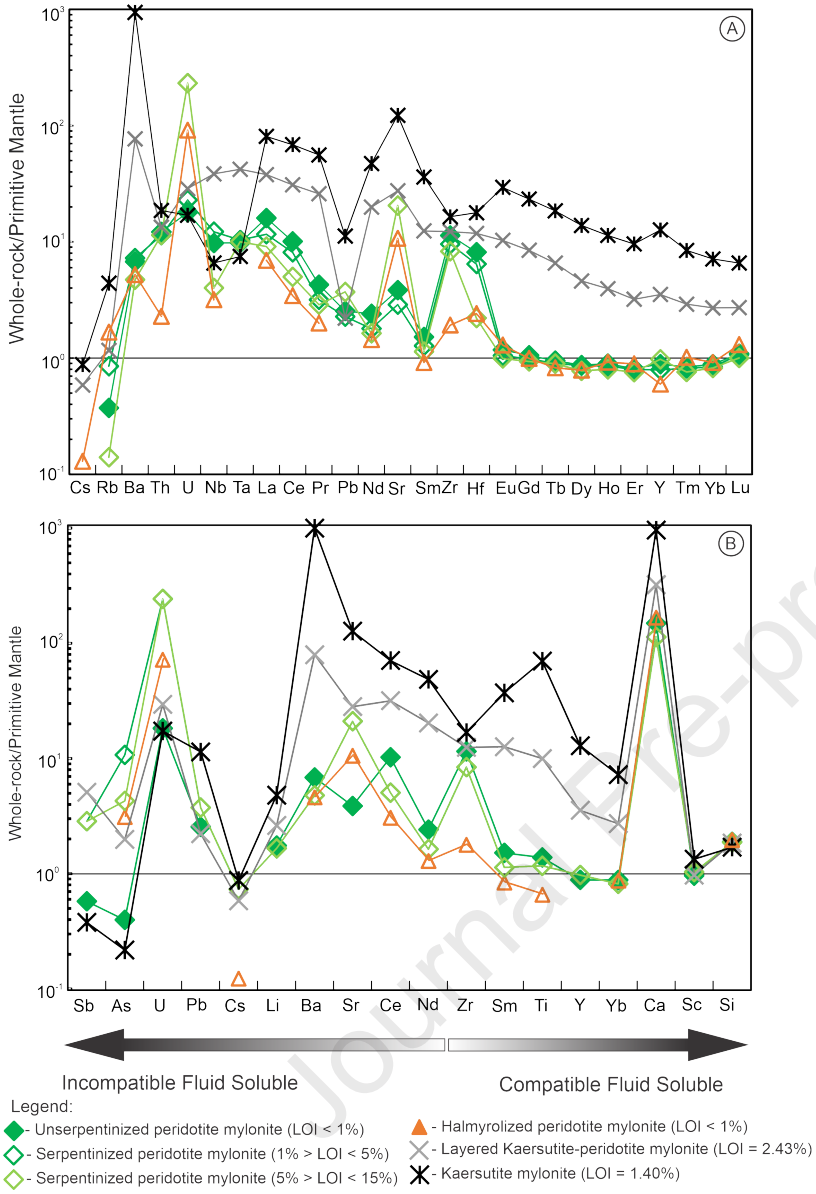

Journal Pre-proof

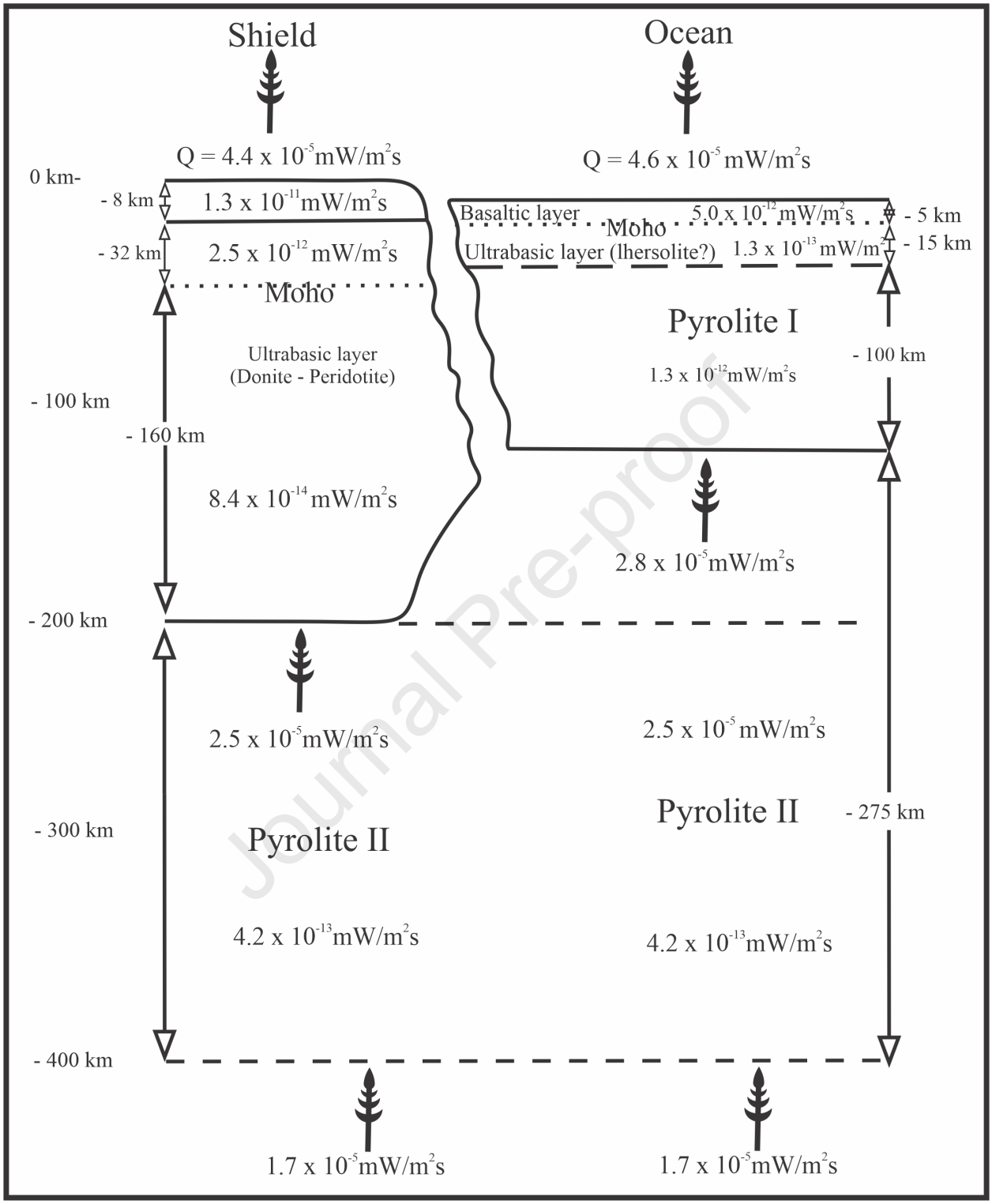

Journal Pre-proof

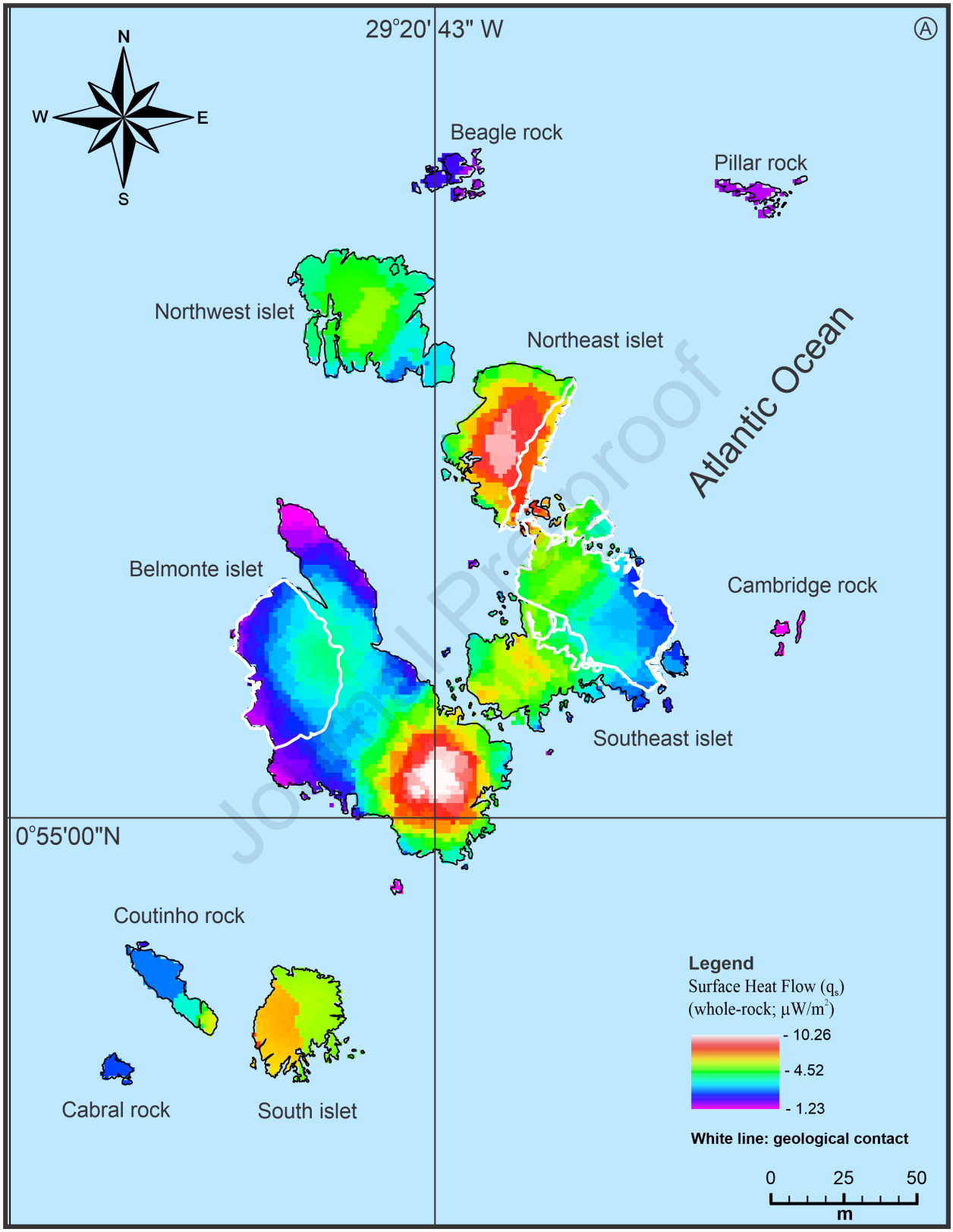

Journal Pre-proof

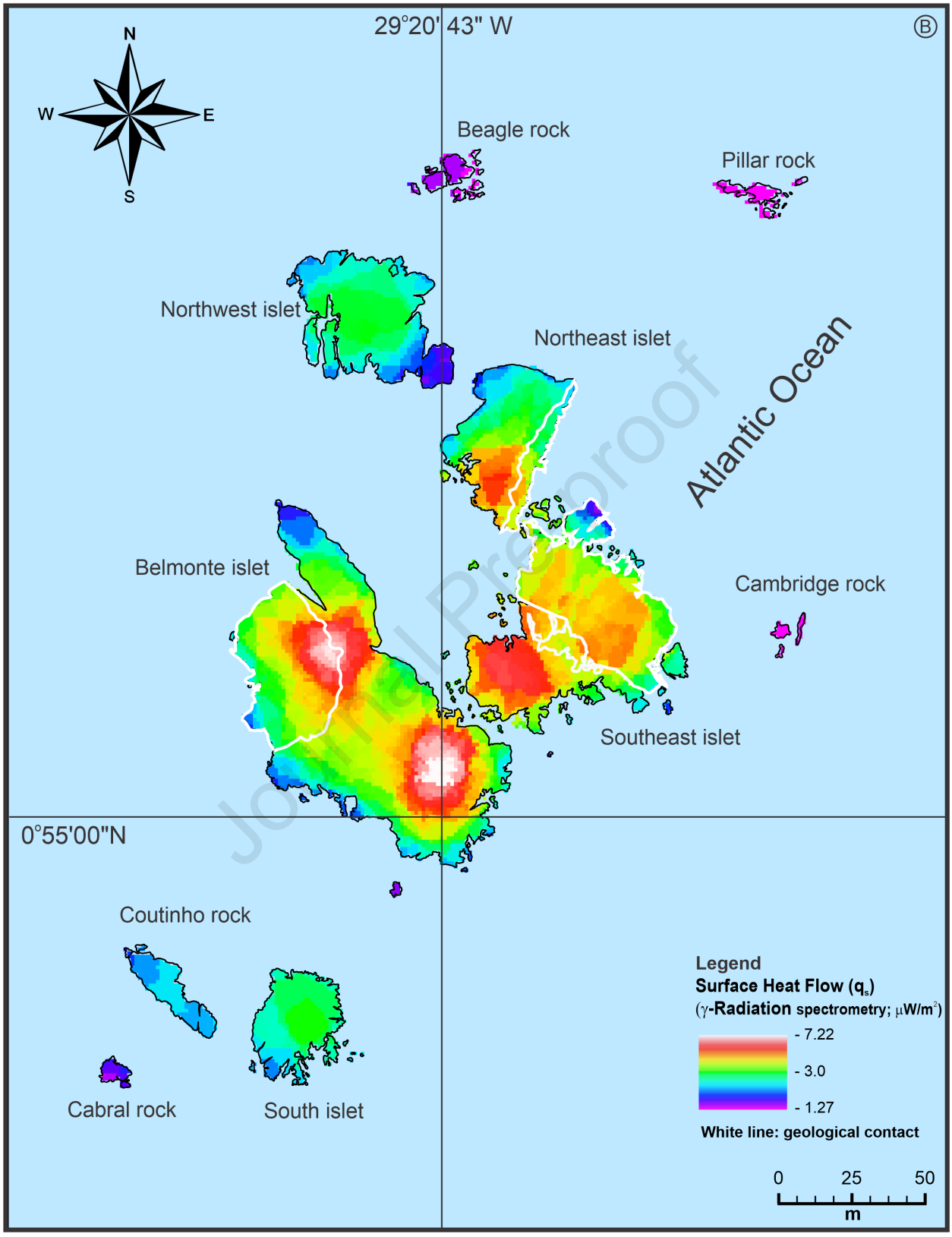

Journal Pre-proof

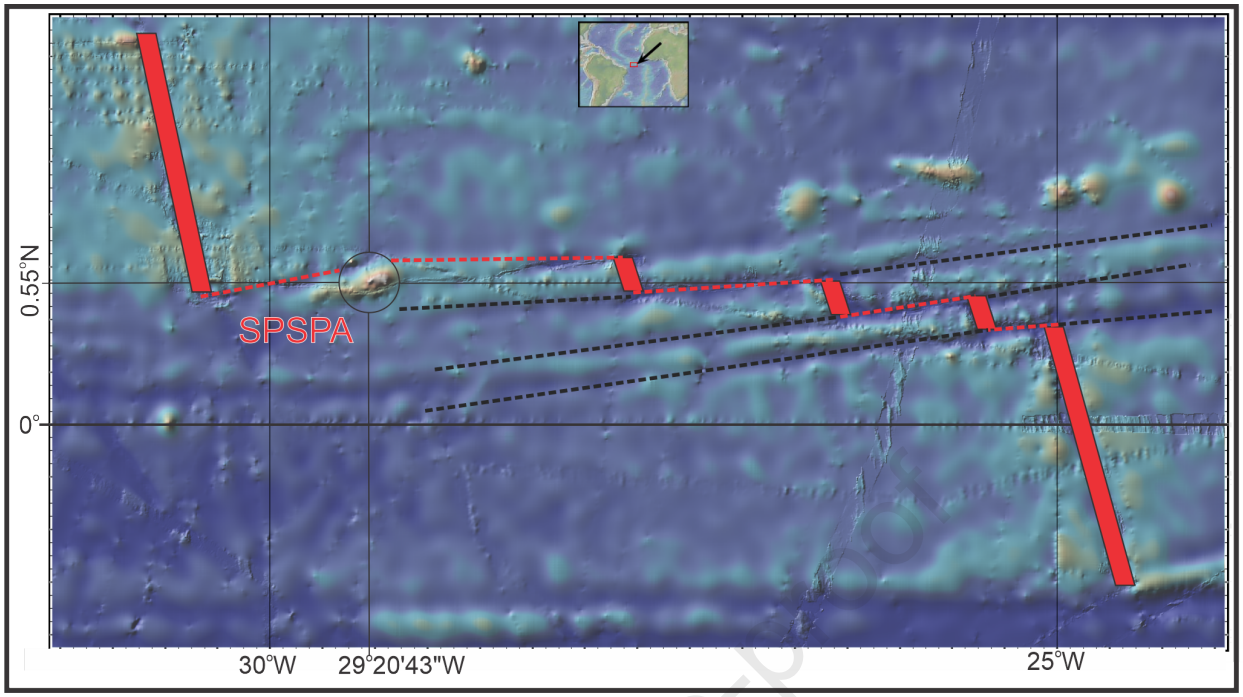

Journal Pre-proof

Journal Pre-proof

Highlights

Surface Radioactive Heat Production and Heat Flow in abyssal mantle rock

Serpentinization, carbonatation process and the hydration of mantle wedge

Serpentinized mantle rock enriched in some incompatible and fluid-mobile elements

Fluid-mobile elements transferred to the mantle wedge by hydrothermal fluids deriving from seawater and oceanic crust

Journal Pre-proof

Journal Pre-proof

Declaration of interests

☒ The authors declare that they have no known competing financial interests or personal relationships that could have appeared to influence the work reported in this paper.

☐The authors declare the following financial interests/personal relationships which may be considered as potential competing interests:

Journal Pre-proof